Article

Tumor cell-intrinsic circular RNA circFNDC3B attenuates CD8+ T cells infiltration in non-small cell lung cancer

Check for updates

Xiaoshan Wei[1,3], Xuan Xiang[1,3], Haolei Wang[1,3], Zihao Wang[1], Shijie Xing[2], Wenbei Peng[1], Linlin Ye[1], Yue Qu[2], Long Chen[1], Bohan Yang[1], Siyu Zhang[1], Qianqian Xue[1], Jiaqi Ai[1], Ke Jiang[2] ✉ & Qiong Zhou[1] ✉

Tumor-infiltrating CD8+ T cells are critical for anti-tumor immunity and positively associated with patient survival. However, the mechanisms governing CD8+ T cell infiltration remain incompletely elucidated, particularly those involving circular RNAs (circRNAs). In this study, we characterized circRNA expression profiles in four paired normal and tumor tissues of non-small-cell lung cancer (NSCLC) and identified that circFNDC3B, a circular transcript derived from exons 2 and 3 of the fibronectin type III domain containing 3B (*FNDC3B*) gene, as significantly upregulated in NSCLC tissues. Mechanistic investigations revealed that circFNDC3B directly binds to transcription factor II-I (TFII-I), forming an RNA-protein complex that competitively disrupts the interaction between TFII-I and STAT1. This sequestration abrogates the transcriptional activation of CXCL10 and CXCL11, two critical chemokines governing CD8+ T cell chemoattraction. Consequently, reduced CXCL10/11 expression significantly impairs CD8+ T cell infiltration into the tumor microenvironment. Consistently, the murine ortholog circFndc3b expression exhibits an inverse correlation with CD8+ T cell infiltration in tumors. Our study uncovers a crucial circRNA-mediated regulatory axis wherein circFNDC3B impedes anti-tumor immunity by suppressing chemokine-dependent CD8+ T cell recruitment, positioning circFNDC3B as a potential therapeutic target to enhance CD8+ T cell-mediated anti-tumor responses in NSCLC.

Lung cancer remains the most prevalent cancer and leading cause of cancer-related mortality worldwide[1]. Non-small-cell lung cancer (NSCLC) accounts for ~85% of lung cancer cases, with lung adenocarcinoma (LUAD) and lung squamous cell carcinoma (LUSC) being the primary subtypes[1]. Despite therapeutic advancements, the prognosis for NSCLC remains dismal, with a 5-year survival rate of only 26% for localized disease and a stark decline to 8% in metastatic cases[2,3]. Immunotherapy has emerged as a pivotal treatment option since the US Food and Drug Administration approved the first immune checkpoint inhibitor in 2015[4,5]. However, its efficacy remains limited, with only 27–46% of patients with advanced NSCLC responding to therapy[6]. Furthermore, among those who initially respond, 65% experience disease progression within 4 years[7]. These limitations underscore the imperative to identify novel therapeutic targets capable of potentiating sustained anti-tumor immunity.

CD8+ T cells serve as crucial immune effectors capable of recognizing and eliminating tumor cells within the tumor microenvironment (TME)[8,9]. Extensive clinical studies have demonstrated a strong positive correlation between CD8+ T cell infiltration and favorable patient outcomes[10]. However, the absence of CD8+ T cells creates an "immune-excluded" TME and hampers the effectiveness of immune checkpoint blockade therapies[10,11]. This immunological barrier is orchestrated by a complex network of immunosuppressive mechanisms, including dysregulated tumor-intrinsic signaling pathways, aberrant chemokine gradients, and stromal-mediated physical barriers[12–14]. These findings underscore an urgent need to elucidate the molecular mechanisms governing CD8+ T cell exclusion and to identify actionable targets for reprogramming immunosuppressive niches in tumors.

CircRNAs, a conserved class of endogenous ncRNAs, are generated through back-splicing mechanisms that produce covalently closed RNA

---

[1]Department of Respiratory and Critical Care Medicine, Union Hospital, Tongji Medical College, Huazhong University of Science and Technology, Wuhan, China. [2]Department of Thoracic Surgery, Union Hospital, Tongji Medical College, Huazhong University of Science and Technology, Wuhan, China. [3]These authors contributed equally: Xiaoshan Wei, Xuan Xiang, Haolei Wang. ✉e-mail: Jiangke@hust.edu.cn; zhouqiongtj@126.com

loops resistant to exonuclease degradation[15]. These molecules exhibit multifaceted regulatory roles in gene expression through diverse mechanisms, including transcriptional modulation, miRNA sponging, RNA-binding protein interactions, and even polypeptide translation[16,17]. Nuclear-localized circRNAs can directly engage with transcription factors to regulate gene expression, either by facilitating the formation of transcriptional complexes or competitively disrupting existing protein-protein interactions[18–20]. Accumulating evidence indicates the crucial roles of circRNAs in shaping anti-tumor immunity through their regulation of CD8^{+} T cell recruitment[21–23]. For example, elevated circIGF2BP3 expression is inversely associated with CD8^{+} T cell infiltration and impairs anti-tumor immunity[24]. CircMGA promotes CD8^{+} T cells infiltration in bladder cancer through upregulation of the chemokine CCL5 by interacting with HNRNPL[23]. Additionally, circFAT1 and circMET have been found to inhibit CD8^{+} T cell infiltration in head and neck squamous cell carcinoma and hepatocellular carcinoma, respectively[25,26]. Despite these advances, the functional landscape of circRNAs in modulating CD8^{+} T cell in NSCLC remains poorly defined, representing a critical knowledge gap in our understanding of immune evasion.

In this study, we investigated the circRNA expression profile in paired tumor and adjacent normal lung tissues from NSCLC patients. We found that circFNDC3B, derived from exons 2 and 3 of the fibronectin type III domain containing 3B (FNDC3B) gene, as significantly upregulated in NSCLC tumor tissues. Mechanistically, we demonstrated that TFII-I functions as a transcriptional activator by interacting with STAT1 to transcriptionally activate CXCL10 and CXCL11, thereby facilitating CD8^{+} T cell infiltration. Strikingly, elevated circFNDC3B competitively binds to TFII-I, disrupting its interaction with STAT1 and consequently inhibiting the transcriptional activation of CXCL10 and CXCL11. This mechanism establishes an immune-excluded TME by impairing CD8^{+} T cell infiltration, ultimately promoting tumor progression. Collectively, our findings propose circFNDC3B as a potential therapeutic target to enhance CD8^{+} T cell infiltration and improve anti-tumor immunity in NSCLC.

Results

CircRNAs landscape in NSCLC tissues
To delineate the circRNA expression landscape in NSCLC, we performed circRNA sequencing on rRNA-depleted total RNA from four pairs of NSCLC tumors and adjacent normal tissues. CircRNAs were identified across various genomic regions (Fig. 1A). In total, 9912 distinct circRNAs were detected, with 9696 containing at least four back-splice junction reads (Fig. 1B). Most circRNAs originated from protein-coding exons, while a smaller fraction mapped to intergenic regions and introns (Fig. S1A). Exonic circRNAs exhibited a median length of ~300 nucleotides, with the majority under 1000 nucleotides (Fig. S1B). Additionally, we found that a single gene could generate multiple circRNAs (Fig. S1C), and 82.3% of exonic circRNAs were composed of 2–4 exons (Fig. S1D). Compared to the circBase database[27], 3340 novel circRNAs and 6572 known circRNAs were identified (Fig. S1E). Furthermore, differential expression analysis revealed that 793 circRNAs were significantly dysregulated in NSCLC tissues, of which 678 were downregulated and 115 upregulated (Figs. 1C and S1F, and Supplementary Data 1 and 2). These findings indicate that circRNAs, as a large RNA family, may contribute to NSCLC progression.

Characterization and expression of circFNDC3B in NSCLC
Among the dysregulated circRNAs, circFNDC3B—derived from exons 2 and 3 of the FNDC3B gene—was the most significantly upregulated in NSCLC tissue compared to adjacent normal lung tissue (log2 fold change = 1.6181, p = 0.0000000111; Figs. 1C and S1F, and Supplementary Data 2). This upregulation was further validated in a larger NSCLC cohort (Fig. 1D). To investigate the specific cellular localization of circFNDC3B within the TME, we conducted in situ hybridization analysis coupled with RT-qPCR quantification in tumor specimens. The results indicated that circFNDC3B was primarily localized in EPCAM^{+} tumor cells and CD45^{−} non-immune cells (Fig. S2A, B). Elevated circFNDC3B expression was also

detected in NSCLC cell lines (A549, H1299, H226, and SPC-A1) compared to human bronchial epithelial cells (HBE) (Fig. S2C). Kaplan-Meier survival analysis further demonstrated that high circFNDC3B expression was associated with worse overall survival (OS) in NSCLC patients (Fig. 1E).

The circular structure of circFNDC3B was confirmed by specifically amplification using divergent primers followed by Sanger sequencing of the head-to-tail junction (Fig. 1F). PCR analysis using genomic DNA (gDNA) and complementary DNA (cDNA) templates demonstrated that circFNDC3B could only be amplified from cDNA, not gDNA, corroborating its back-splicing origin (Figs. 1G and S2D). In addition, circFNDC3B displayed increased stability than linear FNDC3B transcripts when treated with RNase R exonuclease or actinomycin D, further confirming its circular structure (Figs. 1H, I and S2E). Cytoplasmic/nuclear fractionation and FISH analysis showed that circFNDC3B was predominantly localized in the nucleus of NSCLC cells (Figs. 1J, K and S2F). Collectively, these findings establish circFNDC3B as a bona fide circRNA, markedly upregulated in NSCLC cells, suggesting its potential functional role in tumor biology.

### CircFNDC3B has no direct effects on NSCLC cell behaviors
To elucidate the biological function of circFNDC3B, we evaluated its effects on NSCLC cell phenotypes in vitro and in vivo. Overexpression of circFNDC3B produced a 215 bp circRNA (consistent with its expected length) that localized predominantly to the nucleus without altering FNDC3B mRNA (mFNDC3B) levels (Fig. S3A–C). Three shRNAs targeting the splicing site of circFNDC3B were designed, of which sh-circFNDC3B#2 specifically silenced circFNDC3B without affecting mFNDC3B (Fig. S3D). Surprisingly, modulation of circFNDC3B expression had no significant impact on NSCLC cell invasion, apoptosis, cell cycle, or proliferation in vitro (Fig. S3E–K). Consistent findings were observed in an NSCLC xenograft model in NOD-SCID mice, where circFNDC3B expression did not influence tumor growth (Fig. S3L, M).

CircFNDC3B impairs CD8^{+} T cell infiltration via CXCL10/11 suppression
Given the lack of circFNDC3B effects on tumor cell-intrinsic behaviors and the immunodeficient nature of NOD-SCID mice, we hypothesized that circFNDC3B may regulate tumor progression by modulating the immune microenvironment, especially CD8^{+} T cells—the primary mediators of anti-tumor immunity. To test this, activated CD8^{+} T cells from healthy donors were adoptively transferred into tumor-bearing NOD-SCID mice. Interestingly, circFNDC3B overexpression significantly accelerated tumor growth in NOD-SCID mice injected with CD8^{+} T cells (Fig. 2A), indicating that circFNDC3B may promote NSCLC progression by regulating CD8^{+} T cells rather than exerting direct effects on tumor cells.

To systematically investigate the immunoregulatory function of circFNDC3B, we performed transcriptomic profiling in circFNDC3B-overexpressing NSCLC cells. RNA sequencing revealed that circFNDC3B-overexpressing induced significant transcriptional changes in both A549 (255 downregulated and 156 upregulated genes) and H226 cells (161 downregulated and 101 upregulated genes) compared to corresponding control cells (log2 fold change < 1, p < 0.05; Fig. 2B–D and Supplementary Data 3 and 4). Comparative analysis identified a core set of 17 consistently downregulated and 3 upregulated genes across both cell lines (Fig. 2C, D). Notably, we found that CXCL10 and CXCL11, two key chemokines essential for CD8^{+} T cells recruitment[28], were simultaneously downregulated after circFNDC3B overexpression (Fig. 2E). Given the well-established roles of CXCL10 and CXCL11 in promoting CD8^{+} T cell infiltration and anti-tumor immunity, their coordinated downregulation by circFNDC3B provides a plausible molecular explanation for the accelerated tumor progression.

Since various cell types can secrete CXCL10 and CXCL11, we explored their expression in different cell populations in NSCLC samples using the online tool TISCH2 and revealed that macrophages exhibited a higher gene signature than other cells (Fig. 2F). We then isolated 1×10^6 CD45^{−} cells, CD45^{+} cells, and CD14^{+} macrophages from tumor tissues
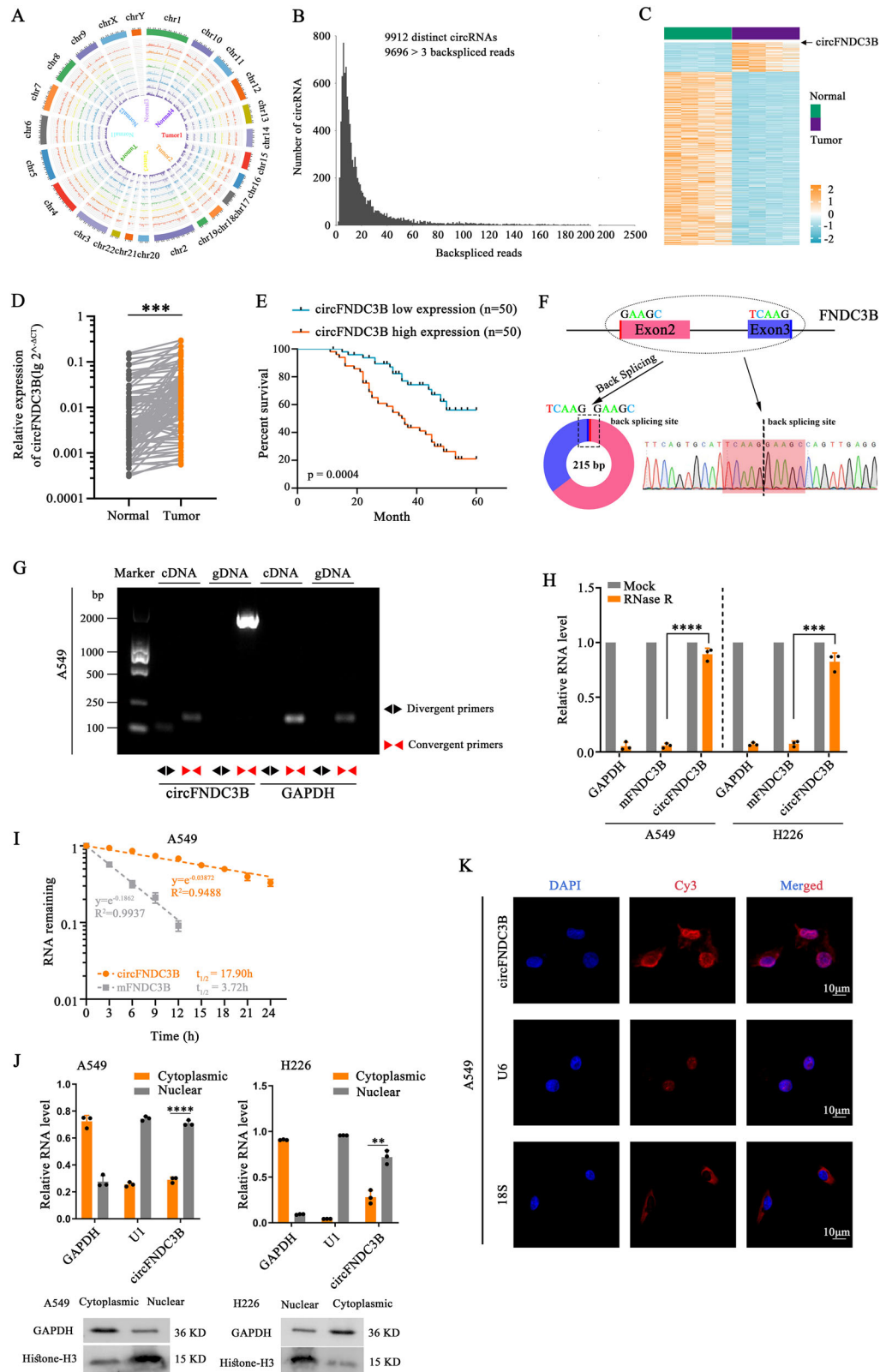
and cultured for 48 h. Enzyme-linked immunosorbent assay (ELISA) results indicated that CD14+ macrophages possessed the highest per-cell chemokine secretion capacity, CD45− cells showed substantial production, and other CD45+ cells contributed minimally (Fig. 2G). However, the proportion of CD14+ macrophages was significantly smaller than that of CD45− cells in the TME (Fig. 2H). These findings collectively demonstrated that while macrophages exhibited superior chemokine-producing capacity on a per-cell basis, the numerical dominance of tumor cells within the TME establishes them as the principal source of CXCL10 and CXCL11. This cellular hierarchy suggests that circFNDC3B-mediated transcriptional repression in tumor cells can substantially alter the chemokine milieu of the TME.

Fig. 1 | Identification and distribution of circFNDC3B. A The outside circle represents gDNA, while the inside circle displays the back-spliced junction reads of circRNAs for each sample. Different sample was represented by different color. **B** The number of back-spliced reads and detected circRNAs was quantified in four paired normal and tumor tissues of NSCLC patients. **C** A heatmap illustrates the differentially expressed circRNAs between the four paired normal and tumor tissues in NSCLC. The columns represent individual tissue samples, while rows correspond to distinct circRNAs. **D** The expression levels of circFNDC3B were measured in 100 paired normal and tumor tissues in NSCLC. Data are displayed as mean ± SD. (Student's t-test, ***$P < 0.001$). **E** NSCLC patients were grouped into circFNDC3B low expression cohort ($n = 50$) and high expression cohort ($n = 50$) based on the median expression level. Kaplan-Meier survival curves were used to compare overall survival between the two groups (Log-rank test). **F** Sequencing analysis confirmed the head-to-tail back-splicing junction of circFNDC3B. **G** Convergent and divergent primers were used to amplify circFNDC3B and GAPDH from cDNA and gDNA in A549 cells. **H** The relative RNA levels of GAPDH, circFNDC3B, and linear FNDC3B (mFNDC3B) were assessed in A549 and H226 cells, treated with or without RNase R. Data were displayed as mean ± SD. (Student's t-test, $n = 3$, ***$P < 0.001$, ****$P < 0.0001$). **I** The stability of circFNDC3B and mFNDC3B was assessed in A549 cells at different time points following Actinomycin D treatment ($n = 3$). **J** RT-qPCR analysis was performed to determine the subcellular distribution of circFNDC3B in the nucleus and cytoplasm of A549 and H226 cells. U1 and GAPDH served as nucleus and cytoplasmic marker, respectively (Student's t-test, $n = 3$, **$P < 0.01$, ****$P < 0.0001$). **K** RNA FISH for circFNDC3B in A549 cells. The positive controls for nucleus and cytoplasm were represented with U6 and 18S, respectively. CircFNDC3B, U6, and 18S probes were labeled with Cy3. Nuclei were stained with DAPI.

We further validated the transcriptomic findings using RT-qPCR and ELISA in both A549 and H226 cells. These experiments confirmed that circFNDC3B overexpression significantly reduced both the mRNA expression and protein secretion of CXCL10 and CXCL11, whereas circFNDC3B knockdown led to opposite effects (Fig. 2I, J). Functional transwell assays demonstrated that circFNDC3B impaired the chemotactic capacity of NSCLC cell-conditioned media toward CD8$^+$ T cells, an effect reversed by circFNDC3B knockdown (Fig. 2K). Collectively, these results establish a mechanistic link between tumor cell-intrinsic circFNDC3B expression and impaired CD8$^+$ T cells infiltration through transcriptional suppression of CXCL10 and CXCL11, highlighting a novel immune evasion pathway in NSCLC pathogenesis.

CircFNDC3B interacts with TFII-I in NSCLC cells

Having established circFNDC3B's role in chemokine regulation, we sought to elucidate the underling mechanism. To determine whether circFNDC3B functions through the canonical miRNA sponge mechanism, we first investigate its miRNA-binding capacity. RNA Immunoprecipitation (RIP) assays revealed no interaction between circFNDC3B and AGO2, excluding a canonical sponge function (Fig. 3A). To further explore the biological function of circFNDC3B in NSCLC cells, we performed RNA pull-down assays using biotin-labeled probes targeting the back-splicing junction of circFNDC3B to identify potential interacting proteins. A specific band was observed on silver-stained sodium dodecyl sulfate-polyacrylamide gel electrophoresis (SDS-PAGE) gels (Fig. 3B). Mass spectrometry analysis identified TFII-I, but not AGO2, as a binding partner of circFNDC3B (Figs. 3C and S4A, B, and Supplementary Data 5). This interaction was further validated by pull-down assay, which selectively captured TFII-I (Fig. 3D). Additionally, RIP assays using purified TFII-I protein confirmed the specific interaction of circFNDC3B and TFII-I (Figs. 3E and S4C). Immunofluorescence staining and RNA fluorescent in situ hybridization (FISH) assays further demonstrated the colocalization of circFNDC3B and TFII-I in NSCLC cells (Fig. 3F). To delineate the structural basis of the interaction between circFNDC3B and TFII-I, we conducted deletion mapping of TFII-I domains (Fig. 3G). Our results revealed that amino acids 102–399 of TFII-I were critical for circFNDC3B binding, whereas deletion of other domains had minimal impact on their interaction (Fig. 3H, I). Interestingly, we noted that TFII-I expression was downregulated in NSCLC tissues and correlated with better survival outcomes (Fig. S4D, E). These findings suggest that TFII-I, particularly its 102–399 amino acids domain, forms a nuclear protein-RNA complex with circFNDC3B in NSCLC cells, potentially playing functional roles in tumor progression.

### CircFNDC3B disrupts TFII-I/STAT1 complex formation

Previous study has shown that TFII-I physically interacts with STAT1 to form a functional protein complex in murine fibroblasts[29], which was independently confirmed by co-immunoprecipitation (Co-IP) assays in human NSCLC cells (Fig. 4A). However, while TFII-I overexpression did not alter the total expression of STAT1, it significantly enhanced STAT1 phosphorylation (Fig. 4B). Analyses of publicly available chromatin immunoprecipitation (ChIP) sequencing data revealed abundant STAT1 binding peaks on the CXCL10 and CXCL11 promoters (Fig. S5A, B). In line with these results, ChIP-qPCR confirmed that STAT1 specifically occupied CXCL10 and CXCL11 promoter regions (Fig. 4C, D). Strikingly, we observed a strong co-binding localization of TFII-I and STAT1 on CXCL10 and CXCL11 promoters (Fig. S5C, D). To further elucidate the regulatory role of TFII-I and STAT1 on CXCL10 and CXCL11 transcriptional activity, we conducted dual-luciferase reporter experiments. Overexpression of TFII-I significantly increased the luciferase activity of CXCL10 and CXCL11 promoters, whereas STAT1 knockdown abrogated this effect (Figs. 4E and S5E, F). Consistently, TFII-I overexpression increased CXCL10 and CXCL11 mRNA levels, while STAT1 silencing counteracted this effect (Fig. S5G). Together, these findings suggest that TFII-I/STAT1 complex functions as a transcriptional activator, facilitating CXCL10 and CXCL11 expression.

Given that circFNDC3B forms a stable RNA-protein complex with TFII-I, we investigated whether circFNDC3B/TFII-I complex might affect the stability of TFII-I/STAT1 complex. Strikingly, circFNDC3B overexpression weakened the interaction between TFII-I and STAT1 (Fig. 4F). Although circFNDC3B overexpression did not alter the total STAT1 levels, it significantly reduced STAT1 phosphorylation, which could be partially rescued by TFII-I overexpression (Fig. 4G). We then examined whether circFNDC3B modulates CXCL10 and CXCL11 expression by interfering with the TFII-I/STAT1 complex. The circFNDC3B-induced decrease in CXCL10 and CXCL11 transcriptional activity was reversed by TFII-I overexpression (Figs. 4H and S5H). In addition, STAT1 overexpression restored CXCL10 and CXCL11 expression, countering the inhibitory effects of circFNDC3B (Figs. 4I and S5I). Taken together, our findings illustrate that circFNDC3B competes with STAT1 for TFII-I binding, thereby suppressing the transcriptional activity of CXCL10 and CXCL11. This reveals a novel regulatory mechanism by which circFNDC3B modulates immune-related gene expression in NSCLC.

CircFNDC3B restricts CD8$^+$ T cell recruitment by disrupting TFII-I/STAT1-dependent chemokine expression

Previous studies have established that CXCL10 and CXCL11 promote the recruitment of CD8$^+$ T cells into the TME[30]. Based on the Tumor-Immune Estimation Resource (TIMER) database[31] (https://cistrome.shinyapps.io/timer/), we found a strong correlation between CD8$^+$ T cell infiltration and CXCL10/CXCL11 expression in both LUAD and LUSC (Fig. 5A). Notably, NSCLC tissues with low circFNDC3B expression exhibit significantly higher CD8$^+$ T cell infiltration compared to those with high circFNDC3B expression (Fig. 5B, C). To further validate these findings, we performed in vitro chemotaxis assays, demonstrating that circFNDC3B overexpression weakened CD8$^+$ T cell migration toward the supernatant of A549 cells. This impaired chemotaxis was restored upon the addition of rhCXCL10 and rhCXCL11 (Fig. 5D). Conversely, circFNDC3B knockdown enhanced CD8$^+$ T cell migration, an effect that was abolished by neutralizing antibodies against CXCL10 and CXCL11 (Fig. 5E). Additionally, the overexpression of either TFII-I or STAT1 reversed the
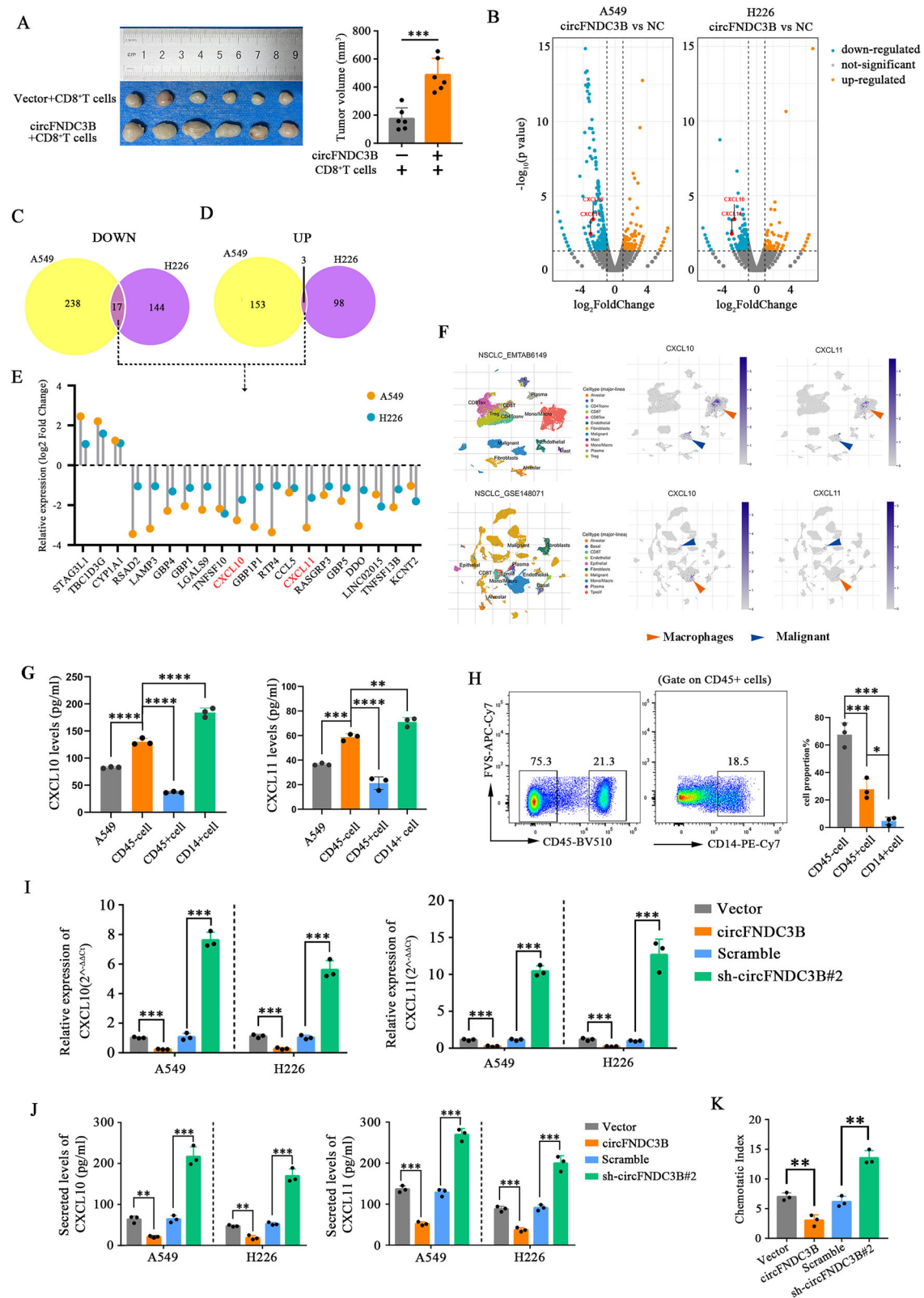
inhibitory effects of circFNDC3B on CD8$^+$ T cell chemotaxis (Fig. 5F, G). Mechanistically, we have demonstrated that tumor cell-intrinsic circFNDC3B functions as a molecular disruptor of the TFII-I/STAT1 transcriptional complex, thereby downregulating CXCL10 and CXCL11 expression and creating an immunosuppressive TME through impaired CD8$^+$ T cell recruitment in NSCLC.

IFN-γ promotes CXCL10 and CXCL11 expression

Activated CD8$^+$ T cells serve as the primary source of secreted IFN-γ[32]. The biological functions of IFN-γ are mediated through its receptor IFNGR1 (IFNGR), which activates the STAT1 signaling pathway to promote anti-tumor immunity[32,33]. Consistent with previous reports[30], we confirmed that IFN-γ upregulated CXCL10 and CXCL11 expression in NSCLC

Fig. 2 | CircFNDC3B impairs CD8⁺ T cell infiltration via CXCL10/11 suppression. A Tumor volume of subcutaneous xenograft in NOD-SCID mice. A549 cells stably transfected with either vector control or circFNDC3B were injected subcutaneously. Purified CD8⁺ T cells from healthy volunteers were intravenously injected into the mice. Data were displayed as mean ± SD. (Student's t-test, $n = 6$, ***$P < 0.001$). **B** Volcano plots depicting differentially expressed genes in A549 and H226 cells transfected with either vector control or circFNDC3B overexpression plasmid. Venn diagrams demonstrate the number of overlapping downregulated (**C**) and upregulated (**D**) genes between A549 and H226 cells. **E** Lollipop chart indicating the relative expression of overlapping genes based on RNA-seq analysis. **F** The analysis of online single-cell RNA sequencing databases TISCH2 showed that CXCL10 and CXCL11 are primarily expressed in macrophages, followed by tumor cells in the TME of NSCLC. **G** The basal expression levels of CXCL10 and CXCL11 in the culture supernatants of A549, CD45⁻ cells, CD45⁺ cells, and CD14⁺ macrophages. Collectively, a total of

1×10^6 CD45⁻ cells, CD45⁺ cells, and CD14⁺ macrophages were sorted by flow cytometry and cultured for 48 h. The culture supernatants were then applied for the measurement of CXCL10 and CXCL11. (one-way ANOVA, $n = 3$, ** $P < 0.01$, *** $P < 0.001$, **** $P < 0.0001$). **H** The proportion of CD45⁺ cells, CD45⁻ cells, and CD14⁺ cells were measured by flow cytometry (one-way ANOVA, $n = 3$, * $P < 0.05$, *** $P < 0.001$). **I** Relative mRNA expression levels of CXCL10 and CXCL11 in A549 cells following circFNDC3B overexpression or knockdown, determined by RT-qPCR. Data were displayed as mean ± SD. (Student's t-test, $n = 3$, *** $P < 0.001$). **J** Secreted CXCL10 and CXCL11 levels were quantified by ELISA. Data were displayed with mean ± SD. (Student's t-test, $n = 3$, ** $P < 0.01$, *** $P < 0.001$). **K** Chemotaxis of CD8⁺ T cells toward the supernatants of A549 cells with circFNDC3B overexpression or knockdown was measured using Transwell assays. Data were displayed as mean ± SD. (Student's t-test, $n = 3$, ** $P < 0.01$).

(Fig. S6A, B). Dual-luciferase reporter assays further revealed that IFN-γ enhanced the transcriptional activity of CXCL10 and CXCL11 promoters, an effect reversed by STAT1 knockdown (Fig. S6C). Notably, IFN-γ reversed circFNDC3B-mediated suppression of CXCL10 and CXCL11 expression (Fig. S6D). Moreover, circFNDC3B knockdown increased CXCL10 and CXCL11 expression, an effect that was further potentiated by IFN-γ treatment (Fig. S6E). Together, these results suggest that NSCLC cells with low circFNDC3B expression secrete higher levels of CXCL10 and CXCL11, facilitating CD8⁺ T cell infiltration. Furthermore, IFN-γ secreted by CD8⁺ T cells promotes CXCL10 and CXCL11 secretion from tumor cells, forming a positive feedback loop that amplifies the anti-tumor immune response. Conversely, high circFNDC3B expression disrupts this loop, thereby limiting CD8⁺ T cell infiltration and contributes to immune evasion in NSCLC.

CircFndc3b promotes tumor progression by inhibiting CD8⁺ T cell infiltration in vivo

Interestingly, human circFNDC3B and its murine homolog circFndc3b exhibit a high degree of sequence conservation (Fig. S7A), suggesting that circFndc3b may exert similar biological functions in mice. FISH assays demonstrated that circFndc3b is predominantly localized in the nucleus of LLC cells (Fig. 6A). RNA pull-down assays using biotin-labeled probes targeting the back-splicing site of circFndc3b, coupled with RIP analysis, validated the specific interaction between circFndc3b and TFII-I in LLC cells (Fig. 6B, C). Further mechanistic studies confirmed that TFII-I overexpression did not alter total STAT1 expression but notably increased STAT1 phosphorylation (Fig. S7B). Consistent with our findings in NSCLC cells, TFII-I forms a protein-protein complex with STAT1 in LLC cells (Fig. 6D). Importantly, circFndc3b overexpression disrupt the interaction between TFIII and STAT1, indicating that the circFndc3b/TFII-I complex competitively inhibits TFII-I and STAT1 binding (Fig. S7C). This inhibitory effect was reversed by TFII-I overexpression, which restored STAT1 phosphorylation diminished by circFndc3b (Fig. S7D). Functionally, circFndc3b overexpression led to a significant downregulation of CXCL10 and CXCL11 in LLC cells, further supporting its regulatory role in this signaling axis (Fig. 6E).

To investigate the in vivo significance of circFndc3b, we established a subcutaneous tumor model by implanting LLC cells with stable circFndc3b overexpression or knockdown into C57BL/6 mice. Compared to the control mice, those implanted with circFndc3b-overexpressing LLC cells exhibited accelerated tumor growth, while mice implanted with circFndc3b-knockdown cells showed significantly reduced tumor volume (Fig. 6F). Consistent with these observations, flow cytometry and immunohistochemistry (IHC) staining revealed that circFndc3b overexpression decreased CD8⁺ T cell infiltration within tumor tissues, whereas circFndc3b knockdown enhanced their accumulation (Fig. 6G, H). We then evaluated the functional capacity of tumor-infiltrating CD8⁺ T cells. Surprisingly, neither circFndc3b overexpression nor knockdown altered the proportion of IFN-γ⁺ CD8⁺ T cells compared to control tumors (Fig. 6I). However, the proportion of IFN-γ⁺ CD8⁺ T cells was significantly higher in circFndc3b-knockdown tumors than in circFndc3b-overexpressing tumors, which may

be attributed to the lower tumor burden in the knockdown group (Fig. 6I). To further investigate whether circFndc3b directly affects CD8⁺ T cell function, we conducted in vitro co-culture experiments. The results exhibited that neither circFndc3b overexpression nor knockdown altered the proportion of IFN-γ⁺ CD8⁺ T cells (Fig. S7E). Considering recent clinical trial evidence supporting the efficacy of immunotherapy in NSCLC patients[34], we explored whether circFndc3b influence the therapeutic response to anti-PD-1 treatment. Notably, circFndc3b overexpression diminished the tumor-suppressive effect of anti-PD-1 therapy (Fig. 6J). Collectively, these findings reveal that circFndc3b promotes tumor progression by inhibiting CD8⁺ T cell infiltration into the TME and may compromise the efficacy of immunotherapy.

Discussion

Limited infiltration of CD8⁺ T cells within tumors has been associated with an immunosuppressive TME, ultimately dampening anti-tumor immunity and contributing to poor clinical outcomes[9,35]. Understanding how tumors hinder CD8⁺ T cell infiltration is crucial for identifying potential therapeutic targets to enhance anti-tumor efficacy. In this study, we identified tumor cell-intrinsic circFNDC3B as a key negative regulator of CD8⁺ T cell infiltration in NSCLC. Mechanistically, circFNDC3B competes with STAT1 for TFII-I binding by forming a circFNDC3B/TFII-I complex, thereby disrupting the TFII-I/STAT1 interaction. This interference suppresses STAT1-mediated transcription of chemokines CXCL10 and CXCL11, which are pivotal in facilitating CD8⁺ T cell recruitment and migration[30]. Consequently, diminished CXCL10 and CXCL11 expression impairs CD8⁺ T cell infiltration, leading to reduced IFN-γ secretion within the TME. This further restricts STAT1 activation in tumor cells, creating a self-reinforcing negative feedback loop that weakens CXCL10 and CXCL11 expression and ultimately blunts anti-tumor immunity (Fig. S8). Importantly, we also confirmed the existence of a murine ortholog of circFNDC3B, termed circFndc3b, in mouse LLC cells. Similar to human circFNDC3B, circFndc3b expression was inversely correlated with CD8⁺ T cell infiltration and impaired anti-tumor efficacy. Our study elucidates the mechanism by which tumor cell-intrinsic circFNDC3B orchestrates the immunosuppressive TME in NSCLC. Moreover, we identify circFNDC3B as a promising therapeutic target to enhance anti-tumor immunity, offering new avenues for immunotherapeutic intervention.

Emerging evidence has established that circRNAs are not merely byproducts of aberrant splicing but instead possess distinct and diverse biological functions[15]. To explore the landscape of circRNAs in NSCLC, we conducted circRNA profiling on paired tumor and adjacent normal lung tissues. Our study, therefore, provides a comprehensive transcriptomic portrait of circRNAs in NSCLC, expanding the current understanding of the complexity and regulatory potential of circRNAs in NSCLC biology. Furthermore, we demonstrated that circFNDC3B was significantly upregulated in NSCLC tissues and was associated with poor patient prognosis. This finding is consistent with previous studies reporting the multifaceted roles of circFNDC3B in various malignancies and non-nonneoplastic diseases[17,36–38]. Importantly, our findings establish circFNDC3B as both a promising
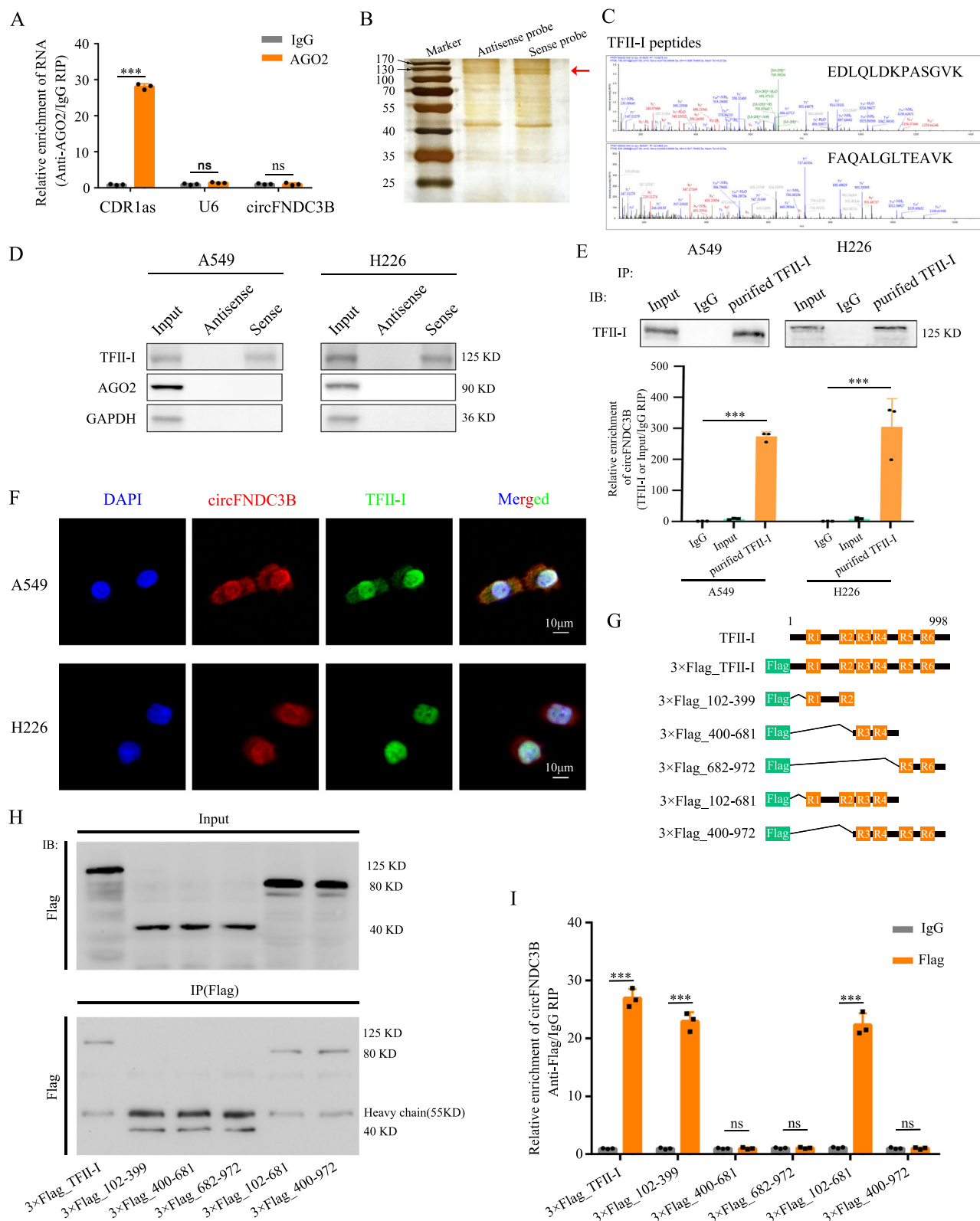
prognostic biomarker and therapeutic target in NSCLC. Future studies with expanded patient cohorts are warranted to fully elucidate the clinical relevance and biological significance of circFNDC3B in NSCLC.

Typically, circRNAs are generated in the nucleus but are primarily localized to the cytoplasm[39]. Studies have indicated that the ATP-dependent RNA helicase DDX39A and DDX39B participate in the nuclear export of circRNAs, with their involvement depending on the length of the circRNA[40].

Additionally, Ngo et al. identified a pathway specifically for the nuclear export of circRNAs, which requires Ran-GTP, exportin-2, and IGF2BP1[41]. However, many circRNAs are retained in the nucleus and are thought to play roles in transcriptional regulation[42]. For example, CircRHOT1 recruit the histone acetyltransferase KAT5 (TIP60) to the NR2F6 protein in the nucleus[43], and CircSEP3 can strongly bind to its cognate DNA, forming an RNA:DNA hybrid and finally leading to the formation of spliced SEP3

Fig. 3 | CircFNDC3B interacts with TFIII in NSCLC cells. A RIP assay with anti-AGO2 or IgG antibodies. U6 and CDR1as were used as negative and positive controls, respectively. Data were displayed with mean ± SD. (Student's t-test, n = 3, ns, not significant, ***P < 0.001). **B** Biotin-labeled antisense or sense circFNDC3B probes were applied for RNA-protein pull-down assay using A549 cell lysates. The silver staining was used to distinguish the proteins interacting with circFNDC3B. The primary differential band precipitated in A549 lysates was indicated by red arrow. **C** The TFII-I peptides pulled down by sense circFNDC3B probes were demonstrated by MS. **D** The interactions between circFNDC3B and TFII-I or AGO2 were detected by RNA pull-down assay and western blot assay in A549 and H226 cells. The loading control was represented with GAPDH. **E** Purified TFII-I protein was preincubated with lysis of A549 and H226 cells. RIP experiments were

performed with IgG and TFII-I antibodies. Utilized the antibodies against TFII-I, the precipitates were subjected to western blot assay. The relative levels of TFII-I-enriched or Input-enriched and IgG-enriched circFNDC3B were determined by RT-qPCR. Data were displayed as mean ± SD. (Student's t-test, n = 3, **P < 0.01, ***P < 0.001). **F** Colocalization of circFNDC3B (red) and TFII-I (green) in A549 and H226 cells was detected by confocal microscopy. Nuclei were stained with DAPI. **G** Schematic diagram displayed full-length and truncated TFII-I protein. **H, I** Flag-tagged domain truncated or full-length TFII-I RIP assays in A549 cells. Using anti-Flag antibody, the precipitate was subjected to western blot assay (**H**). Relative enrichment of endogenous circFNDC3B was analyzed by RT-qPCR (**I**). Data were displayed as mean ± SD. (Student's t-test, n = 3, ns, not significant, **P < 0.01).

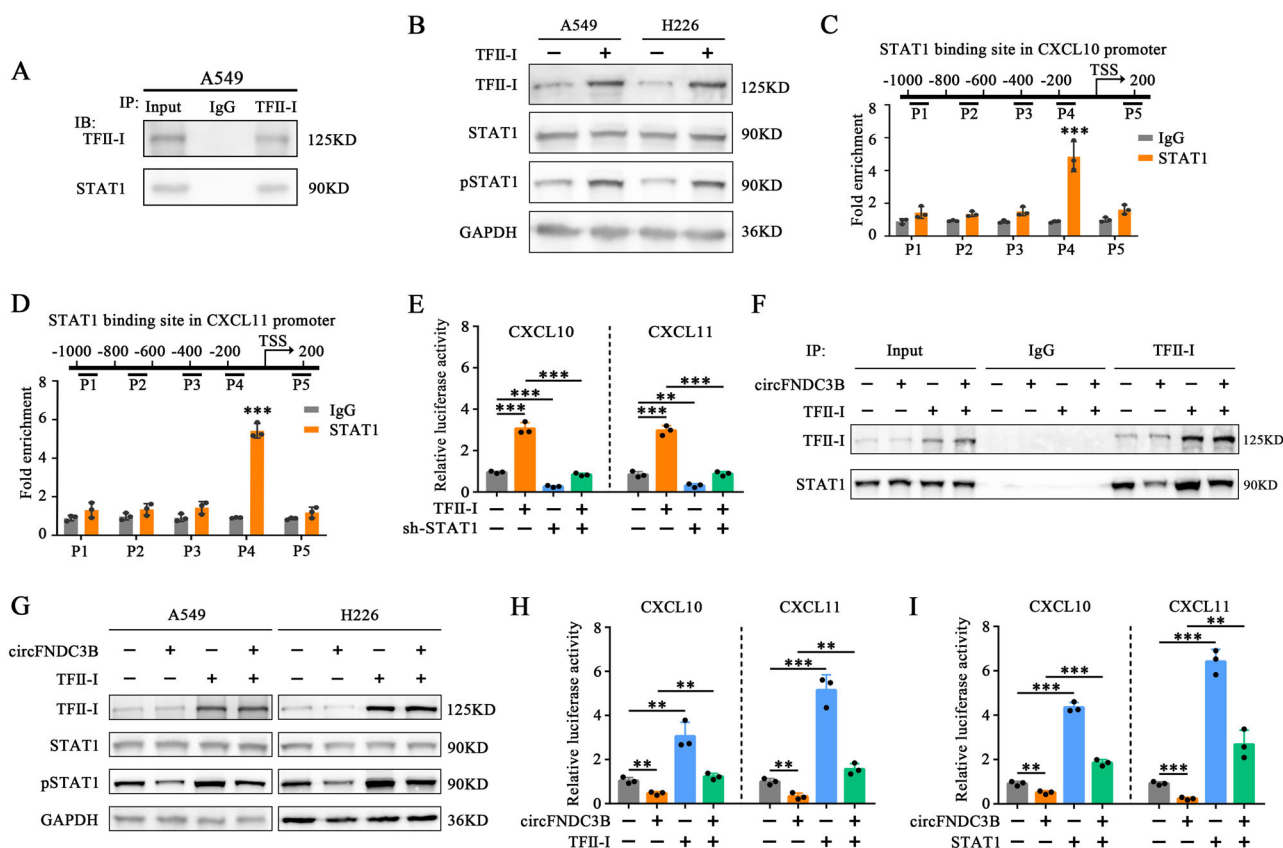**Fig. 4 | CircFNDC3B disrupts TFII-I/STAT1 complex formation. A** Co-IP experiments using anti-TFII-I or IgG antibody detected the interaction between TFII-I and STAT1 in A549 cells. **B** Western blot assay using the indicated antibodies in A549 or H226 cells stably transfected with vector control or TFII-I overexpression plasmid. The enrichment of CXCL10 (**C**) and CXCL11 (**D**) promoter fragments with anti-STAT1 or IgG antibody by ChIP-qPCR in A549 cells. Data were displayed with mean ± SD. (Student's t-test, n = 3, ***P < 0.001). **E** CXCL10 or CXCL11 promoter luciferase activities were determined after knockdown of STAT1 or overexpression of TFII-I in A549 cells. Data were displayed as mean ± SD. (Student's t-test, n = 3, **P < 0.01, ****P < 0.0001). **F** Co-IP experiments about the interaction between

TFII-I and STAT1 using anti-TFII-I antibody after overexpression of circFNDC3B or TFII-I in A549 cells. **G** Western blot assay using the indicated antibodies in A549 cells stably transfected with or without circFNDC3B and TFII-I overexpression plasmids. **H** CXCL10 or CXCL11 promoter luciferase activities were analyzed in A549 cells stably transfected with or without circFNDC3B and TFII-I overexpression plasmids. Data were displayed as mean ± SD. (Student's t-test, n = 3, **P < 0.01, ***P < 0.001). **I** CXCL10 or CXCL11 promoter luciferase activities were analyzed in A549 cells which were stably transfected with or without circFNDC3B and STAT1 overexpression plasmids. Data were displayed as mean ± SD. (Student's t-test, n = 3, **P < 0.01, ***P < 0.001).

mRNA with exon skipping[44]. In our study, we found that circFNDC3B was primarily localized in the nucleus, which may be related to its ability to bind proteins and regulate transcriptional activity. However, the precise molecular determinants (e.g., sequence motifs or structural features) governing circFNDC3B nuclear retention remain uncharacterized. Addressing this gap could inform strategies to modulate its subcellular localization for therapeutic purposes.

In some contexts, circFNDC3B (also known as circ0001361) has been reported to function as a miRNA sponge[39]. For instance, in bladder cancer, circFNDC3B sequesters miR-491-5p, thereby promoting metastasis and invasion through upregulation of MMP9[45]. However, our data suggest that

both anti-AGO2 RIP assays and mass spectrometry analysis following circFNDC3B pulldown failed to detect any interaction between circFNDC3B and AGO2, indicating that circFNDC3B does not engage the miRNA-mediated silencing complex. Moreover, in our NSCLC model, we observed no evidence supporting a role for circFNDC3B in regulating invasion in vitro. Instead, our findings reveal that circFNDC3B exerts its biological functions by directly binding to TFII-I, supporting the emerging concept that circRNAs can regulate gene expression through RNA-protein interactions independent of miRNA sponging[15]. Interestingly, circFNDC3B has also been reported to interact with FUS to regulate VEGF expression, thereby promoting lymphangiogenesis and metastasis in oral squamous cell

A CD8+ T cell immune infiltration in NSCLC

B circFNDC3B low | circFNDC3B high

C

D

E

F

G
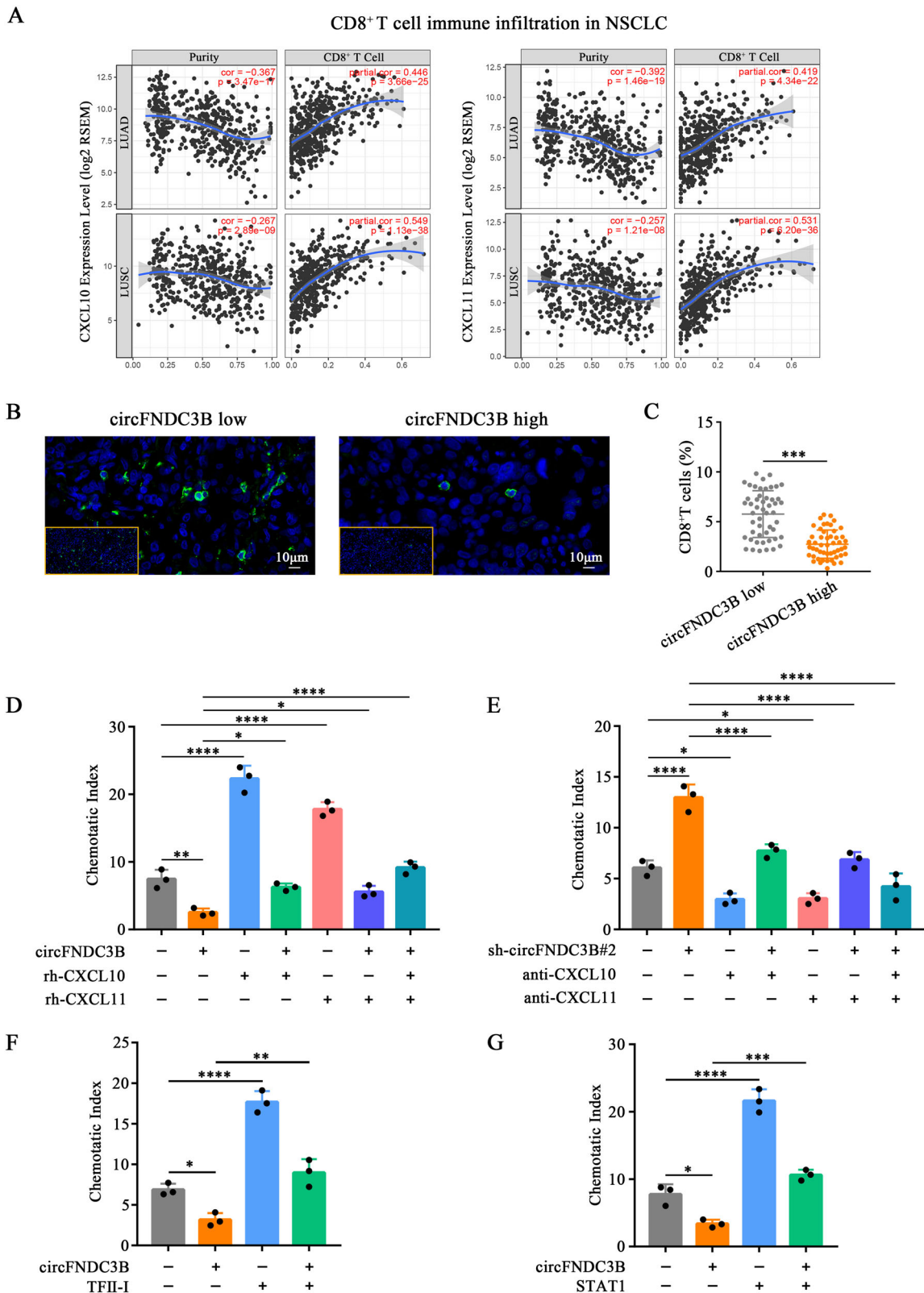
carcinoma[38,46]. However, in our NSCLC model, circFNDC3B does not form a stable interaction with FUS, suggesting that the functional roles of circFNDC3B may be context-dependent and influenced by tissue or cell-type specificity. This functional plasticity highlights the need for systematic characterization of circRNA interactomes across cancer types to identify conserved versus context-specific mechanisms.

The core structure of TFII-I consists of a nuclear localization signal (NLS), a basic region (BR) DNA-binding domain, and multiple protein-protein interaction domains, including a leucine zipper (LZ) and six helix-loop-helix (HLH)-like domains, also known as I-repeats (R1–R6)[47,48]. This structural composition suggests that TFII-I can engage in both protein-protein and protein-DNA interactions. Specifically, the NLS and BR are

Fig. 5 | CircFNDC3B attenuates CD8$^+$ T cells infiltration through TFII-I /STAT1/CXCL10-CXCL11 axis. A The correlation of CXCL10 or CXCL11 expression with tumor purity or CD8$^+$ T cells infiltration (Tumor-immune estimation resource, TIMER) (https://cistrome.shinyapps.io/timer/). **B** IF staining of CD8 (green) in sections of NSCLC tissues with high or low circFNDC3B expression. Nuclei were stained with DAPI. **C** The proportion of CD8$^+$ T cells in sections of NSCLC samples with low ($n = 50$) or high ($n = 50$) circFNDC3B expression. Patients were divided into groups by the median circFNDC3B expression. The proportion of CD8$^+$ T cells were analyzed by ImageJ following the standard protocols and tutorials provided by the software. Data were displayed as mean ± SD. (Student's t-test, ***$P < 0.001$). **D** The chemotaxis of CD8$^+$ T cells towards the supernatants of A549 cells stably overexpressing circFNDC3B or control vector with or without rhCXCL10 and rhCXCL11 treatment. Data were displayed as mean ± SD, (one-way ANOVA, $n = 3$, *$P < 0.05$, **$P < 0.01$, ***$P < 0.001$, ****$P < 0.0001$). **E** The chemotaxis of CD8$^+$ T cells towards the supernatants of A549 cells after circFNDC3B knockdown with or without anti-CXCL10 and anti-CXCL11 treatment. Data were displayed as mean ± SD. (one-way ANOVA, $n = 3$, **$P < 0.01$). **F** The chemotaxis of CD8$^+$ T cells towards the supernatants of A549 cells preferentially transfected with either circFNDC3B or TFII-I overexpression plasmids. Data were displayed as mean ± SD. (one-way ANOVA, $n = 3$, **$P < 0.01$, ***$P < 0.001$). **G** The chemotaxis of CD8$^+$ T cells towards the supernatants of A549 cells preferentially transfected with either circFNDC3B or STAT1 overexpression plasmids. Data were displayed as mean ± SD. (one-way ANOVA, $n = 3$, **$P < 0.01$, ***$P < 0.001$).

located between the R1 and R2 domains. The peptide region spanning amino acids 102–399 lies within this interval and is responsible for mediating both DNA and protein interactions. In contrast, the regions spanning amino acids 400–681 and 682–972, corresponding to R3–R4 and R5–R6, respectively, are primarily involved in protein-protein interaction but lack DNA-binding capacity. In our study, we demonstrated that the peptide region spanning amino acids 102–399 of TFII-I is indispensable for its interaction with circFNDC3B, although TFII-I lacks a canonical RNA-binding domain. However, the precise molecular mechanism underlying this interaction remains unclear. Further structural studies are need to elucidate the molecular basis of the circFNDC3B-TFII-I interaction.

Our findings provide novel insights into the functional domains of TFII-I and their potential involvement in RNA-binding activity. TFII-I is recognized as an atypical transcription factor due to its modular structure and functional versatility. Its HLH-like domains enable dynamic protein-protein interactions, allowing TFII-I to act as both a basal transcription factor and a context-dependent transcriptional repressor or activator through the recruitment of co-repressors or co-activators[48]. In addition, genome-wide association analysis have revealed the dual regulatory role of TFII-I, showing no clear correlation between its genomic binding sites and gene expression patterns[49,50]. Consistent with previous reports[29], we confirmed that TFII-I directly binds to STAT1 in NSCLC, where it collaborats to promote the formation of gene-specific transcriptional activator complexes that drive CXCL10 and CXCL11 transcription. Notably, our study identified circFNDC3B as a critical regulatory partner that competitively disrupts the TFII-I/STAT1 interaction, thereby inhibiting downstream chemokine transcription and impairing CD8$^+$ T cell infiltration. These results highlight a previously unrecognized layer of transcriptional regulation mediated by circFNDC3B and TFII-I. However, the paradoxical observation that TFII-I exhibits tumor-suppressive prognostic value despite its pro-transcriptional role in CXCL10/11 regulation warrants further investigation into its context-dependent functions during NSCLC progression. Further studies are needed to investigate the genome-wide target genes of TFII-I in NSCLC and to delineate the molecular signaling pathways governing its dynamic interactions with transcriptional partners.

Tumor-infiltrating CD8$^+$ T cells are central mediators of anti-tumor immunity and serve as critical determinants of immunotherapy efficacy and patient survival[51]. In this study, we identified the circFNDC3B/TFII-I complex as a key regulator that impedes CD8$^+$ T cell infiltration by inhibiting STAT1 activation in NSCLC, emphasizing the importance of circRNAs in modulating tumor-immune microenvironment. This findings aligns with growing evidence that circRNAs can influence immune cell infiltration and regulate immune responses within the TME[22,26]. Through in vivo functional studies, we demonstrated that circFNDC3B not only inhibited CD8$^+$ T cell infiltration but also accelerated tumor progression. Notably, we observed that circFNDC3B overexpression significantly attenuated the tumor-suppressive effects of anti-PD-1 therapy. However, it is important to acknowledge that our assessment of anti-PD-1 efficacy was primarily based on tumor growth measurements under a single treatment protocol, without comprehensive characterization of the immune landscape before and after therapy. Specifically, we lacked longitudinal profiling of T cell infiltration, T cell exhaustion markers, and regulatory T cell dynamics,

which limits our ability to draw definitive conclusions about the causal role of circFNDC3B in modulating anti-PD-1 responsiveness. To address these limitations, future studies should incorporate combinatorial treatment strategies involving circFNDC3B inhibition alongside PD-1 blockade, complemented by high-dimensional immune profiling to capture spatial and temporal changes in immune cell populations. Additionally, single-cell transcriptomic analyses could offer mechanistic insights into how circFNDC3B reshapes tumor–immune interactions at molecular resolution. Crucially, the clinical relevance of these findings warrants further validation in patient-derived organoid models or humanized mouse systems.

Nevertheless, our study still has several limitations that warrant consideration. First, the initial circRNA screening was conducted in a small cohort ($n = 4$ paired samples), which may limit the generalizability of circFNDC3B as a broadly applicable biomarker across NSCLC subtypes. Future studies involving larger, well-annotated patient cohorts stratified by histological subtypes and molecular characteristics are needed to validate its clinical relevance. Second, the translational relevance of our findings is limited by the use of immunodeficient NOD-SCID mice for in vivo validation. Although adoptive transfer of CD8$^+$ T cells partially recapitulates key aspects of the human TME, the absence of functional innate immune components—such as natural killer (NK) cells and macrophages—may fail to fully capture the complexity of tumor-immune interactions. Lastly, although we demonstrated that circFNDC3B suppresses the expression of CXCL10 and CXCL11, the functional requirement of their receptor, CXCR3, on CD8$^+$ T cells has not been directly tested. Genetic ablation or pharmacological inhibition of CXCR3 would provide critical mechanistic evidence linking circFNDC3B-driven chemokine suppression to impaired T cell recruitment.

Conclusion
In summary, our study reveals a previously unrecognized, tumor cell-intrinsic mechanism by which circFNDC3B drives immunosuppression in NSCLC. Specifically, we demonstrate that circFNDC3B disrupts the TFII-I/STAT1 transcriptional complex, thereby inhibiting CXCL10/11-mediated CD8$^+$ T cell recruitment. These findings broaden the functional landscape of circRNAs in cancer biology, highlighting their ability to directly modulate transcriptional regulation through RNA–protein interactions, beyond the conventional paradigm of miRNA sponging. Importantly, we identify circFNDC3B as a therapeutic target, whose inhibition may enhance the anti-tumor-immune efficacy.

Methods
Tissues and cell lines
Tumor tissues (T) and paired adjacent normal tissues (N) were collected from NSCLC patients undergoing surgery at the Department of Thoracic Surgery, Union Hospital, Tongji Medical College, Huazhong University of Science and Technology, between July 2014 and December 2018. Written informed consent was obtained from all participants and the study was approved by the Institutional Review Board of the Tongji Medical College of Huazhong University of Science and Technology. All ethical regulations relevant to human research participants were followed. All NSCLC tissues were snap-frozen in liquid nitrogen and stored at -80℃ until used. Histopathological confirmation of all samples was performed using hematoxylin and eosin
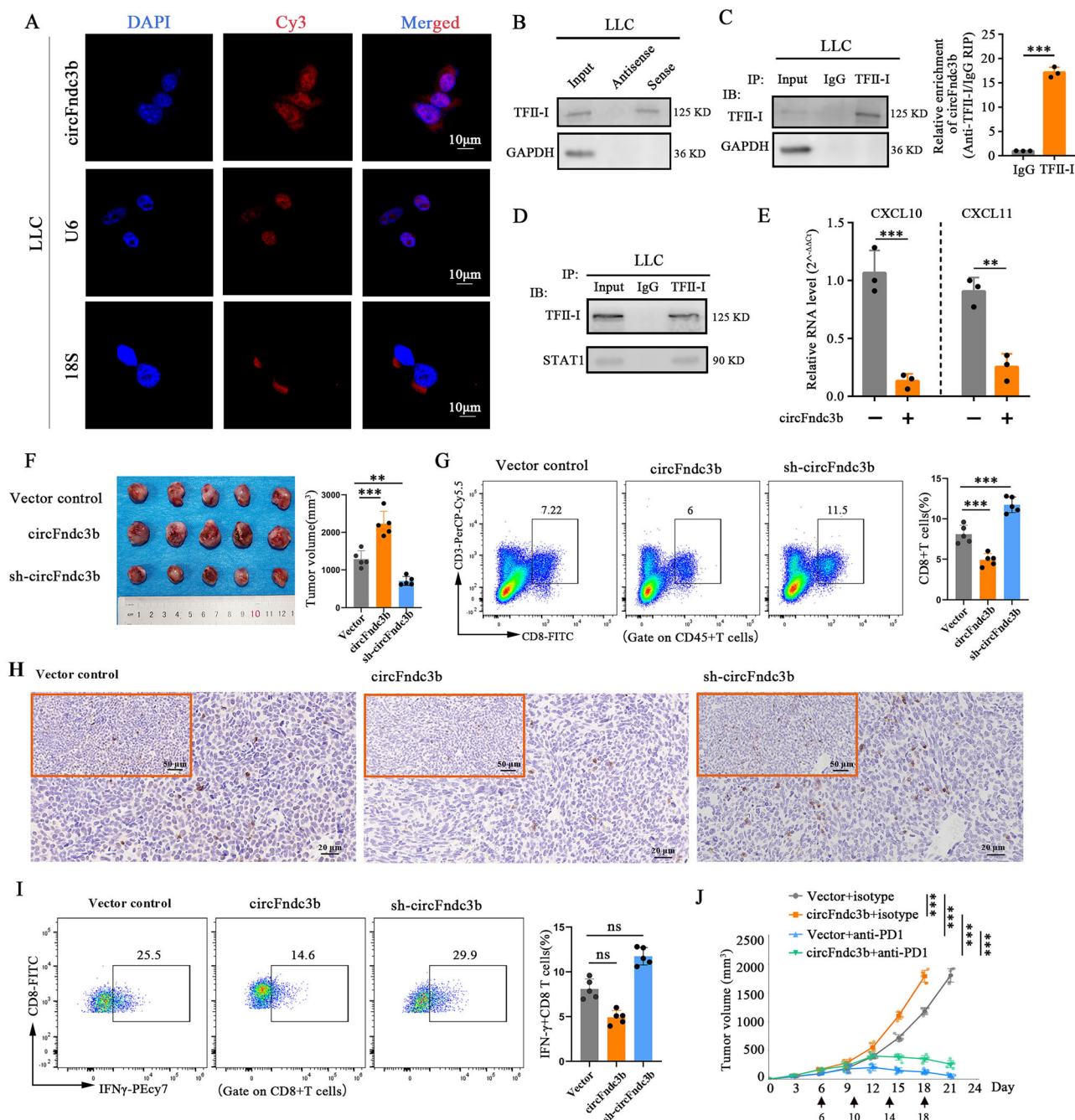
Fig. 6 | CircFndc3b promotes tumor progression by inhibiting CD8$^+$ T cell infiltration in vivo. A RNA FISH for circFndc3b in LLC cells. The positive controls for nucleus and cytoplasm were represented with U6 and 18S, respectively. CircFndc3b, U6, and 18S probes were labeled by Cy3. Nuclei were stained with DAPI. **B** The RNA-protein pull-down experiments with biotin-labeled sense or antisense circFndc3b probes in LLC cell lysates. The loading control was provided with GAPDH. **C** RIP assays with anti-TFII-I and anti-IgG antibodies were performed in LLC cell lysates. The precipitates were subjected to Western blot assay. The relative levels of TFII-I enriched and IgG-enriched circFndc3b were determined by RT-qPCR. Data were displayed as mean ± SD. (Student's t-test, $n = 3$, **$P < 0.01$, ***$P < 0.001$). **D** Co-IP experiments using anti-TFII-I and IgG antibodies detected the interaction between TFII-I and STAT1 in LLC cells. **E** The relative mRNA levels of CXCL10 and CXCL11 in LLC cells overexpressing circFndc3b were determined by RT-qPCR. Data were displayed as mean ± SD. (Student's t-test, $n = 3$, **$P < 0.01$,

***$P < 0.001$). **F** The tumor volumes were measured following subcutaneous injection of LLC cells with stable circFndc3b overexpression, knockdown, or vector control into C57BL/6 mice. Data were displayed as mean ± SD. (one-way ANOVA, $n = 5$, ** $P < 0.01$, *** $P < 0.001$). **G** The frequency of CD3$^+$ CD8$^+$ T cells in LLC tumors with either circFndc3b overexpression or knockdown was analyzed using flow cytometry. Data were displayed as mean ± SD. (one-way ANOVA, $n = 5$, *** $P < 0.001$). **H** IHC staining for CD8$^+$ T cells in sections from LLC tumors with either circFndc3b overexpression or knockdown. **I** The proportion of IFN-γ$^+$ CD8$^+$ T cells was analyzed using flow cytometry. (one-way ANOVA, $n = 5$, ns: no significance). **J** The growth curves of the subcutaneous LLC tumor in C57BL/6 mice. Isotype or anti-PD-1 was administered intraperitoneally at the indicated time (arrows, Day 6, Day 10, Day 14, and Day 18). Data were displayed as mean ± SD. (Student's t-test, $n = 6$, ***$P < 0.001$).

(H&E)-stained sections. Clinical characteristics of the cohort are summarized in Table S1. All patients were followed up regularly, and OS time was determined from the date of surgery to the date of death or last follow-up.

The human NSCLC cell lines A549 (RRID: CVCL_0023), NCI-H1299 (RRID: CVCL_0060), NCI-H226 (RRID: CVCL_1544), and SPC-A1 (RRID: CVCL_6955); human bronchial epithelial cell line HBE1 (RRID: CVCL_0287), and murine Lewis lung cancer cell line LL/2 (LLC; RRID: CVCL_4358) were purchased from the American Type Culture Collection (Manassas, USA). H1299, H226, SPC-A1, and HBE cells were cultured in Roswell Park Memorial Institute 1640 (RPMI-1640; ThermoFisher, Waltham, USA) medium supplemented with 10% fetal bovine serum (FBS; ThermoFisher, Waltham, USA). A549 cells were cultured in Ham's F-12K (Kaighn's; ThermoFisher, Waltham, USA) medium supplemented with 10% FBS (ThermoFisher), and LLC cells were cultured in Dulbecco's modified Eagle's medium (DMEM, ThermoFisher, Waltham, USA) supplemented with 10% FBS (ThermoFisher). All cells were incubated at 37 °C with 5% CO_2 and authenticated within the past 3 years. All experiments were performed with mycoplasma-free cells.

Identification and annotation of human NSCLC circRNAs
Total RNA was extracted from four paired NSCLC and adjacent normal lung tissues using the RNeasy Mini Kit (Qiagen, Hilden, Germany) according to the manufacturer's instructions. Ribosomal RNA (rRNA) was depleted using the RiboZero rRNA Removal Kit (Illumina, San Diego, USA), followed by linear RNA digestion with RNase R (Illumina, San Diego, USA). Enriched circRNAs were fragmented, reverse-transcribed into cDNA with random primer and sequenced on the Illumina NovaSeq 6000 platform (Illumina, USA). CircRNAs were identified using find_circ[52] and CIRI2[53]. Differential expression analysis between tumor and normal tissues was performed with DESeq (version 1.10.1), and adjusted P-values were calculated using the Benjamini-Hochberg method. Raw RNA-seq data are available in the SRA database (accession code: PRJNA863919).

RNA preparation, RNase R treatment, and RT-qPCR
Total RNA from tissues or cells was isolated using the RNeasy Mini Kit (Qiagen). Nuclear and cytoplasmic fractions were separated with the PARIS Kit (ThermoFisher, Waltham, USA). For RNase R treatment, 1 µg total RNA was incubated with or without 3 U of RNase R (Illumina, San Diego, USA) at 37 °C for 15 min. Reverse transcription was performed using PrimeScript RT Master Mix (Takara, Dalian, China), followed by quantitative PCR (qPCR) with SYBR Premix Ex Taq II (Takara, Dalian, China). Divergent primers targeting circRNA junction sites were used for circRNA quantification. gDNA was extracted using a Genomic DNA Isolation Kit (Sangon Biotech, Shanghai, China). The cDNA and gDNA PCR products were visualized using 2% agarose gel electrophoresis. Amplification and cycle thresholds (Ct) analysis were performed on a StepOne Plus Real-Time PCR system (Applied Biosystems, USA). Primers sequences are demonstrated in Supplementary Data 6.

Actinomycin D treatment and RNA stability assay
Cells were seeded in six-well plates for the actinomycin D (Sigma-Aldrich, St. Louis, USA) experiments. Once they reached 60% confluency after 24 h, the cells were treated with 5 µg/mL of actinomycin D or dimethyl sulfoxide (DMSO; Sigma-Aldrich, St. Louis, USA) and collected at indicated time points. The RNA turnover rate and half-life were estimated according to a previously published method[54].

FISH
Cy3-labeled circFNDC3B and circFndc3b probes (Supplementary Data 6) were synthesized by TSINGKE (Wuhan, China). FISH was performed as previously described with minor modifications[55]. Briefly, cancer cells were fixed, permeabilized, and then hybridized with the probes at 37 °C overnight in the dark. The coverslips were washed thrice with 2× saline-sodium citrate (SSC; Solarbio, Beijing, China) for 10 min before being sealed with parafilm containing 4′,6-diamidino-2-phenylindole (DAPI; Roche Diagnostic,

Mannheim, Germany). Images were captured with a confocal laser scanning microscope (LSM 780, Germany).

FISH and Immunocytofluorescence
Fresh tumor samples were fixed in 4% paraformaldehyde for 24 h, dehydrated, and embedded in paraffin. Then, sections were cut, deparaffinized, and rehydrated. After antigen retrieval, the sections were permeabilizing with 0.1% Triton X-100, incubated with phosphate-buffered saline (PBS) containing 5% bovine serum albumin (BSA) to block non-specific binding, and then hybridized with the probes at 37 °C overnight in a dark. The sections were washed three times with 2× SSC (Solarbio, Beijing, China) for 10 min for 3 times on the other day. Next, the sections were incubated with primary antibodies overnight at 4 °C and corresponding secondary antibodies for 1 h at room temperature. Finally, the sections were washed with PBS before they were sealed with parafilm containing DAPI (Roche Diagnostic). Images were captured using a confocal laser scanner (LSM 780, Germany).

CCK-8 assay
Cell viability was accessed using the Cell Counting Kit-8 (CCK-8; Dojindo, Kumamoto, Japan) following the manufacturer's instructions. Absorbance at 450 nm was measured with Synergy 4 microplate reader (BioTek, Winooski, USA).

Transwell Matrigel invasion assay
Invasion assay were performed using Matrigel-precoated Transwell chambers following the manufacturer's protocol (BD Science, Bedford, USA). Homogeneous single-cell suspensions (1×10^5 cells/well) were added to the upper chambers and incubated for 24 h. The invasion rates were quantified by counting the invaded cells at least three random fields per chamber.

Apoptosis assay
Cell apoptosis was detected using the FITC Annexin V Apoptosis Detection Kit I (BD Science, Bedford, USA) according to the manufacturer's instructions. The data were analyzed using the FCS Express 5 software (De Novo Software, Los Angeles, USA).

Cell cycle assay
Cells were fixed in 75% ice-cold ethanol overnight at 4 °C. After washing with PBS, the fixed cells were stained with propidium iodide (PI) buffer (BD Science, Bedford, USA). The cell cycle was examined using flow cytometer, and the data were analyzed using ModFit LT 5.0 software.

RNA-seq
Total RNA from circFNDC3B-overexpressing and control A549/H226 cells was isolated using RNeasy Mini Kit (Qiagen). The library preparations were conducted using the NEBNext® Ultra™ RNA Library Prep Kit for Illumina® (New England Biolabs, Ipswich, USA). Gene expression profiles were determined by Illumina high-throughput RNA sequencing at Novogene (Beijing, China). Significantly differentially expressed transcripts were defined as $p < 0.05$ and $\log_2$(fold change) ≥ 1.

ELISA
CXCL10 and CXCL11 levels in cell culture supernatants were determined using commercially available ELISA kits (Biolegend, San Diego, USA and Raybiotech, Norcross, USA) following the manufacturer's instructions.

RNA pull-down assays
Biotin-labeled oligonucleotide probes targeting the circRNA junction site (sense) and control antisense probes (Supplementary Data 6) were synthesized by TSINGKE. For RNA pull-down assay, 1×10^7 cells were washed with ice-cold PBS, and lysed in 500 µL of Co-IP buffer (20 mM Tris-HCL [pH 7.5], 150 mM NaCl, 1 mM EDTA, 0.5% NP-40) containing protease inhibitors cocktail and RNase inhibitors. Lysates were then incubated with

3 μg biotin-labeled circFNDC3B (sense) or control (antisense) probes for 2 h at room temperature. Next, 50 μL washed streptavidin C1 magnetic beads (Invitrogen, Waltham, USA) were added to each binding reaction and incubated at room temperature for 1 h. After washing with the Co-IP buffer for five times, the bead-bound proteins were eluted for mass spectrometry or western blot analysis.

Silver staining and mass spectrometry analysis
Silver staining was performed using the PAGE Gel Silver Staining Kit (Solarbio, Beijing, China) based on the manufacturer's protocol. Mass spectrometry analysis was performed by Novogene, with protein identification and quantification using Proteome Discoverer software (version 1.4; USA).

Western blot and Co-IP
For western blotting, cells were lysed in RIPA buffer containing protease inhibitors (Beyotime, Nangtong, China). Proteins were size-separated by SDS-PAGE gels and transferred to polyvinylidene difluoride membranes. After blocking with 5% non-fat milk, the membranes were incubated with the primary antibodies at 4 °C overnight and then horseradish peroxidase (HRP)-conjugated secondary antibodies at room temperature for 1 h. Signals were detected using a High-Sensitive ECL Chemiluminescence Detection Kit (Vazyme, Nanjing, China).

For Co-IP assay, cells were lysed in Co-IP buffer containing protease inhibitor cocktail on ice for 40 min. Cell lysates were incubated with the corresponding antibodies adsorbed to protein A/G Agarose (ThermoFisher, Waltham, USA) for 4 h at 4 °C. Then, the cell lysates were washed thrice with Co-IP buffer and eluted at 95 °C for 10 min.

Primary antibodies against the following proteins were used: TFII-I (Santa Cruz Biotechnology, Santa Cruz, USA, 1:500), AGO2 (ThermoFisher, Waltham, USA, 1:500), STAT1 (Abcam, Cambridge, UK, 1:1000), pSTAT1 (Abcam, Cambridge, UK, 1:1000), Flag tag (Abcam, Cambridge, UK, 1:1000), GAPDH (Proteintech, Chicago, USA, 1:50000) and histone-H3 (Proteintech, Chicago, USA, 1:1000). The following HRP-conjugated secondary antibodies were used: goat anti-mouse (Proteintech, Chicago, USA, 1:2000), goat anti-rabbit (Proteintech, Chicago, USA, 1:2000), mouse anti-rabbit IgG heavy chain specific (Proteintech, Chicago, USA, 1:5000) and mouse anti-rabbit IgG light chain specific (Proteintech, Chicago, USA, 1:4000).

RIP
RIP experiment was conducted using the Magna RIP RNA-Binding Protein Immunoprecipitation Kit (Millipore, Bedford, USA) according to the manufacturer's instructions. Cell lysates were incubated with Dynabeads coated with antibodies against AGO2 (ThermoFisher, Waltham, USA, 8 μg), TFII-I (Santa Cruz Biotechnology, 1 μg), Flag tag (Abcam, 1 μg) or Mouse IgG (Santa Cruz Biotechnology, Dallas, USA, 1 μg) antibody at 4 °C overnight. The co-precipitated RNAs were purified using RNeasy MinElute Cleanup Kit (Qiagen, Hilden, Germany) and detected by RT-qPCR.

Immunocytofluorescence
Cells were grown on coverslips and fixed with 4% paraformaldehyde. After permeabilizing with 0.1% Triton X-100, the cells were washed with PBS, blocked with 5% BSA, and incubated with TFII-I antibody (Santa Cruz Biotechnology, 1:500) overnight. Subsequently, the cells were washed with PBS and incubated with a fluorophore-labeled secondary antibody (Abcam, 1:500). Finally, the cells were sealed with parafilm containing DAPI. Fluorescence images were captured using a confocal laser scanner, and the data were analyzed using ImageJ software.

Vector construction and transfection
To establish circFNDC3B, circFndc3b, TFII-I, and STAT1 overexpression plasmids, circFNDC3B, circFndc3b, TFII-I, and STAT1 cDNA were synthesized by TSINGKE (Wuhan, China) and then cloned into pcDNA3.1(+) CircRNA Mini Vector (Addgene, Watertown, USA) and p3×FLAG-CMV-10 vector (Sigma-Aldrich, St. Louis, USA), respectively. The truncations of

TFII-I were constructed as regions spanning amino acids 102–399 (3×Flag_102–399), 400–681 (3×Flag_400–681), 682–972 (3×Flag_682–972), 102–681 (3×Flag_102–681), and 400–972 (3×Flag_400–972). TFII-I truncations were FLAG-tagged in p3×FLAG-CMV-10 vector. Oligonucleotides encoding short hairpin RNAs (shRNAs, Supplementary Data 6) specific for circFNDC3B, circFndc3b, and STAT1 were cloned into pLKO.1-puro plasmid (Sigma-Aldrich, St. Louis, USA).

Cells were transfected with the vectors using Lipofectamine 2000 (Life Technologies, Carlsbad, USA) according to the manufacturer's instructions. Stable cell lines were screened by administering neomycin or puromycin (Invitrogen, Carlsbad, USA). Scramble shRNAs and empty vectors were used as controls.

CHIP and qPCR (ChIP-qPCR) assays
ChIP assays were performed using the EZ-Magna ChIP A/G Chromatin Immunoprecipitation Kit (Sigma-Aldrich, St. Louis, USA). First, the DNA fragments were resuspended in PBS and incubated with anti-STAT1 (Abcam, 5 μg) or rabbit IgG (Abcam, 5 μg) antibodies at 4 °C overnight. The precipitated DNA-chromatin complexes were analyzed by qPCR, and data were demonstrated as fold enrichment normalized to IgG. The primer sequences used for ChIP-qPCR are listed in Supplementary Data 6.

Dual-luciferase reporter assay
A549 cells were co-transfected with reporter constructs for CXCL10 or CXCL11 promoter (−1000 to 300 bp) in pGL3-Basic vector, with the Renilla luciferase reporter vectors pRL-TK as the internal control. After 24 h, firefly and Renilla luciferase activities were quantified using Dual-Luciferase® Reporter Assay System (Promega, Madison, USA) according to the manufacturer's protocol.

CD8$^+$ T cells isolation
Peripheral blood mononuclear cells from healthy donors were isolated using Ficoll-Hypaque gradient centrifugation. Purified CD8$^+$ T cells were isolated using the Human CD8$^+$ T cells Isolation Kit (Miltenyi Biotec, Teterow, Germany) according to the manufacturer's protocol. The CD8$^+$ T cells were >90% pure, as confirmed by flow cytometry. Purified CD8$^+$ T cells were cultured in RPMI-1640 medium supplemented with 10% FBS. The medium contained recombinant human IL-2 (Abcam, Cambridge, UK, 10 ng/mL), soluble anti-human CD28 mAbs (Biolegend, San Diego, USA, 1 μg/mL), and plate-bound anti-human CD3 mAbs (Biolegend, San Diego, USA, 1 μg/mL). The cells were then cultured for three consecutive days for the subsequent experiments.

Tumor dissociation and cell sorting
Fresh human NSCLC tumor tissues were cut into small pieces and digested with DNase I (Sigma-Aldrich, St. Louis, USA, 50 μg/mL) and collagenase type IV (ThermoFisher, Waltham, USA, 200 U/mL) at 37 °C for 60 min. Then, the single-cell suspensions were resuspended in PBS and incubated with surface antibodies anti-human CD45 (Biolegend, San Diego, USA) and anti-human CD14 (Biolegend, San Diego, USA) in the dark for 30 min. Subsequently, the prepared cells were sorted using fluorescence-activated cell sorting (FACS) by BD FACSAria II Cell Sorter.

Chemotaxis assay
Pre-activated CD8$^+$ T cells were resuspended in RPMI-1640 medium supplemented with 0.5% FBS and placed in the upper chamber of Transwell tissue culture inserts (5.0 μm pore diameter; Corning, New York, USA). Supernatant from A549 cells was added to the lower chamber. RPMI-1640 medium alone was used as the negative control. When indicated, anti-CXCL11 (R&D Systems, Minneapolis, USA, 1 μg/mL), anti-CXCL10 (R&D Systems, Minneapolis, USA, 1 μg/mL), recombinant human (rh)-CXCL11 (R&D Systems, Minneapolis, USA, 50 ng/mL), or rhCXCL10 (R&D Systems, Minneapolis, USA, 50 ng/mL) were added to the lower chamber. Then, the chambers were incubated at 37 °C with 5% CO_2 for 4 h. Transmigrated cells in the lower chamber were collected and stained with

anti-human CD8 mAbs (Biolegend, San Diego, USA). After staining, precision count beads (Biolegend, San Diego, USA) were added, and the numbers of transmigrated CD8$^+$ T cells were determined using flow cytometry (FACS Canto II; BD Science, USA). The chemotactic index was calculated as the ratio of the number of CD8$^+$ T cells that migrated to corresponding wells divided by the number of CD8$^+$ T cells that migrated to the wells containing RPMI-1640 medium alone.

In vivo tumorigenesis assays

The NOD-SCID mice or C57BL/6 female mice (4 weeks old) were obtained from Beijing Vital River Laboratory Animal Technology Co., Ltd. (Beijing, China). The mice were housed under specific pathogen-free conditions (25 °C, 12/12-h light/dark cycle) and fed a chow diet in Tongji Medical College Animal Care Facility. All animal experiments were approved by the Animal Care and Utilization Committee of Tongji Medical College, Huazhong University of Science and Technology (number 2021 IECS 2974). We have complied with all relevant ethical regulations for animal use.

In the NOD-SCID mouse experiments, circFNDC3B overexpression and control A549 cells (2×10^6 cells) were subcutaneously injected into the right and left flanks of the same NOD-SCID mice, respectively ($n = 6$). For some experiments, the mice were injected weekly with purified human CD8$^+$ T cells (1×10^7 per mouse) via the tail vein ($n = 6$) beginning 1 week before inoculation with tumor cells. After 4 weeks, the mice were euthanatized, and the tumors were dissected. The volumes of the dissected tumors were measured using calipers and calculated using the formula: $a^2 \times b \times 0.5$ (a is the smallest diameter and b is the diameter perpendicular to a).

In the C57BL/6 mouse experiments, circFndc3b overexpression or knockdown LLC cells (5×10^5 cells) were subcutaneously injected into the right flank of mice ($n = 5$ for each group). After 4 weeks, the mice were euthanatized, and the tumors were dissected. The volumes of the dissected tumors were determined as mentioned above.

In the anti-PD-1 antibody treatment experiments, circFndc3b overexpression and control LLC cells (5×10^5 cells) were subcutaneously injected into the right flank of C57BL/6 mice ($n = 6$/group) on day 0. Then, the mice were injected with anti-mouse PD-1 mAbs (Biolegend, San Diego, USA) or isotype control (Biolegend, San Diego, USA) via tail vein (100 μg/dose) every 4 days for 4 times, beginning on day 6. The tumors were assessed with calipers every 3 days. Tumor volumes were measured as mentioned above. When the tumors reached a maximum of 2000 mm^3, the mice were euthanized.

CD8$^+$ T cell infiltrating analysis

Tumors were digested with DNase I (Sigma-Aldrich, 50 μg/mL) and collagenase type IV (ThermoFisher, 200 U/mL) at 37 °C for 20 min. In order to obtain a single-cell suspension, the cells were filtered (70 μm) to remove clumps and then diluted in medium. Then, the cells were surface-stained with anti-mouse CD45 mAbs (Biolegend, San Diego, USA), anti-mouse CD3 mAbs (Biolegend, San Diego, USA), anti-mouse CD8 mAbs (Biolegend, San Diego, USA), and anti-mouse IFN-γ mAbs (Biolegend, San Diego, USA) for flow cytometry analysis. The data was analyzed using FlowJo_v10.8.1.

IHC staining

Mouse tumors were fixed in 4% paraformaldehyde for 24 h, dehydrated, and embedded in paraffin. Sections were then cut, deparaffinized, and rehydrated. After antigen retrieval, the sections were incubated with PBS containing 5% BSA to block non-specific binding. Next, the sections were incubated with the primary antibody at 4 °C overnight and then the secondary antibody at room temperature for 1 h. After washing with PBS, the sections were treated with streptavidin-peroxidase solution for 30 min and then with diaminobenzidine for 5 min at room temperature.

Co-culture assay

Splenic cell suspensions were prepared by grinding mouse spleens using a 40 mm nylon cell strainer. After separation with lymphoprep, immune cells were collected and cultured in RPMI-1640 medium supplemented with 10% FBS and activated by anti-CD3 (2 mg/mL) and anti-CD28 (5 mg/mL) antibodies for 48 h. Subsequently, 1×10^6 LLC cells (circFndc3b overexpression or knockdown) were co-cultured with the activated immune cells for an additional 48 h, after which flow cytometry was employed to analyze IFN-γ$^+$ CD8$^+$ T cells.

Statistics and reproducibility

All statistical analyses were performed using SPSS Statistics (version 26.0) and GraphPad Prism (version 8.0.2). Continuous variables are presented as mean ± standard deviation (SD). Data were compared using two-tailed Student's t-test between two groups and one-way analysis of variance (ANOVA) between multiple groups. OS was estimated using Kaplan-Meier curves with log-rank tests. The sample sizes and experiment replicates were determined and conducted independently as described in the corresponding "Methods" sections. P-value < 0.05 was considered statistically significant for all analyses and significance levels are presented as $*P < 0.05$, $**P < 0.01$, $***P < 0.001$, and $****P < 0.0001$.

Reporting summary

Further information on research design is available in the Nature Portfolio Reporting Summary linked to this article.

Data availability

The datasets used and/or analyzed during the current study are available from the corresponding author upon reasonable request. Numerical source data for graphs are available in Supplementary Data 7. Uncropped blots are provided in Fig. S9, and the flow cytometry gating strategy is provided in Fig. S10. Raw RNA-seq data are available in the SRA database (accession code: PRJNA863919).

References

1. Siegel, R. L., Miller, K. D., Wagle, N. S. & Jemal, A. Cancer statistics, 2023. *CA Cancer J. Clin.* **73**, 17–48 (2023).
2. Thai, A. A., Solomon, B. J., Sequist, L. V., Gainor, J. F. & Heist, R. S. Lung cancer. *Lancet* **398**, 535–554 (2021).
3. Bai, Y. et al. Immunotherapy for advanced non-small cell lung cancer with negative programmed death-ligand 1 expression: a literature review. *Transl. Lung Cancer Res.* **13**, 398–422 (2024).
4. Kazandjian, D. et al. FDA Approval Summary: nivolumab for the treatment of metastatic non-small cell lung cancer with progression on or after platinum-based chemotherapy. *Oncologist* **21**, 634–642 (2016).
5. Ettinger, D. S. et al. NCCN Guidelines® Insights: non-small cell lung cancer, Version 2.2023. *J. Natl. Compr. Cancer Netw.* **21**, 340–350 (2023).
6. Livanou, M. E., Nikolaidou, V., Skouras, V., Fiste, O. & Kotteas, E. Efficacy of NSCLC rechallenge with immune checkpoint inhibitors following disease progression or relapse. *Cancers* **16**, https://doi.org/10.3390/cancers16061196 (2024).
7. Antonia, S. J. et al. Durvalumab after chemoradiotherapy in Stage III non-small-cell lung cancer. *N. Engl. J. Med.* **377**, 1919–1929 (2017).
8. van der Leun, A. M., Thommen, D. S. & Schumacher, T. N. CD8(+) T cell states in human cancer: insights from single-cell analysis. *Nat. Rev. Cancer* **20**, 218–232 (2020).
9. St Paul, M. & Ohashi, P. S. The roles of CD8(+) T cell subsets in antitumor immunity. *Trends Cell Biol.* **30**, 695–704 (2020).
10. Gueguen, P. et al. Contribution of resident and circulating precursors to tumor-infiltrating CD8(+) T cell populations in lung cancer. *Sci. Immunol.* **6**, https://doi.org/10.1126/sciimmunol.abd5778 (2021).
11. Giles, J. R., Globig, A. M., Kaech, S. M. & Wherry, E. J. CD8(+) T cells in the cancer-immunity cycle. *Immunity* **56**, 2231–2253 (2023).

12. Ford, K. et al. NOX4 inhibition potentiates immunotherapy by overcoming cancer-associated fibroblast-mediated CD8 T-cell exclusion from tumors. *Cancer Res.* **80**, 1846–1860 (2020).

13. Shang, S. et al. TRIB3 reduces CD8(+) T cell infiltration and induces immune evasion by repressing the STAT1-CXCL10 axis in colorectal cancer. *Sci. Transl. Med.* **14**, eabf0992 (2022).

14. Spranger, S., Bao, R. & Gajewski, T. F. Melanoma-intrinsic beta-catenin signalling prevents anti-tumour immunity. *Nature* **523**, 231–235 (2015).

15. Liu, C. X. & Chen, L. L. Circular RNAs: characterization, cellular roles, and applications. *Cell* **185**, 2016–2034 (2022).

16. Chen, L. L. The expanding regulatory mechanisms and cellular functions of circular RNAs. *Nat. Rev. Mol. Cell Biol.* **21**, 475–490 (2020).

17. Sun, K. et al. Emerging landscape of circFNDC3B and its role in human malignancies. *Front. Oncol.* **13**, 1097956 (2023).

18. Chen, Q. et al. Circular RNA ACTN4 promotes intrahepatic cholangiocarcinoma progression by recruiting YBX1 to initiate FZD7 transcription. *J. Hepatol.* **76**, 135–147 (2022).

19. Wu, N. et al. YAP circular RNA, circYap, attenuates cardiac fibrosis via binding with tropomyosin-4 and gamma-actin decreasing actin polymerization. *Mol. Ther.* **29**, 1138–1150 (2021).

20. Fang, L., Du, W. W., Awan, F. M., Dong, J. & Yang, B. B. The circular RNA circ-Ccnb1 dissociates Ccnb1/Cdk1 complex suppressing cell invasion and tumorigenesis. *Cancer Lett.* **459**, 216–226 (2019).

21. Zhang, Q. et al. Roles of circRNAs in the tumour microenvironment. *Mol. Cancer* **19**, 14 (2020).

22. Li, B. et al. circNDUFB2 inhibits non-small cell lung cancer progression via destabilizing IGF2BPs and activating anti-tumor immunity. *Nat. Commun.* **12**, 295 (2021).

23. Sun, J. et al. Regulation of CD8(+) T cells infiltration and immunotherapy by circMGA/HNRNPL complex in bladder cancer. *Oncogene* **42**, 1247–1262 (2023).

24. Liu, Z. et al. N(6)-methyladenosine-modified circIGF2BP3 inhibits CD8(+) T-cell responses to facilitate tumor immune evasion by promoting the deubiquitination of PD-L1 in non-small cell lung cancer. *Mol. Cancer* **20**, 105 (2021).

25. Huang, X. Y. et al. Circular RNA circMET drives immunosuppression and anti-PD1 therapy resistance in hepatocellular carcinoma via the miR-30-5p/snail/DPP4 axis. *Mol. Cancer* **19**, 92 (2020).

26. Jia, L., Wang, Y. & Wang, C. Y. circFAT1 promotes cancer stemness and immune evasion by promoting STAT3 activation. *Adv. Sci.* **8**, 2003376 (2021).

27. Glazar, P., Papavasileiou, P. & Rajewsky, N. circBase: a database for circular RNAs. *RNA* **20**, 1666–1670 (2014).

28. Karin, N. CXCR3 ligands in cancer and autoimmunity, chemoattraction of effector T cells, and beyond. *Front. Immunol.* **11**, 976 (2020).

29. Kim, D. W., Cheriyath, V., Roy, A. L. & Cochran, B. H. TFII-I enhances activation of the c-fos promoter through interactions with upstream elements. *Mol. Cell. Biol.* **18**, 3310–3320 (1998).

30. Tokunaga, R. et al. CXCL9, CXCL10, CXCL11/CXCR3 axis for immune activation — a target for novel cancer therapy. *Cancer Treat. Rev.* **63**, 40–47 (2018).

31. Li, T. et al. TIMER: a web server for comprehensive analysis of tumor-infiltrating immune cells. *Cancer Res.* **77**, e108–e110 (2017).

32. Wang, W. et al. CD8(+) T cells regulate tumour ferroptosis during cancer immunotherapy. *Nature* **569**, 270–274 (2019).

33. Spens, A. E., Sutliff, N. A., Bennett, S. R., Campbell, A. E. & Tapscott, S. J. Human DUX4 and mouse Dux interact with STAT1 and broadly inhibit interferon-stimulated gene induction. *eLife* **12**, https://doi.org/10.7554/eLife.82057 (2023).

34. Reck, M., Remon, J. & Hellmann, M. D. First-line immunotherapy for non-small-cell lung cancer. *J. Clin. Oncol.* **40**, 586–597 (2022).

35. Anandappa, A. J., Wu, C. J. & Ott, P. A. Directing traffic: how to effectively drive T cells into tumors. *Cancer Discov.* **10**, 185–197 (2020).

36. Zhao, Y. et al. CircFndc3b mediates exercise-induced neuroprotection by mitigating microglial/macrophage pyroptosis via the ENO1/KLF2 axis in stroke mice. *Adv. Sci.* **12**, e2403818 (2025).

37. Chen, Z. et al. CircFNDC3B regulates osteoarthritis and oxidative stress by targeting miR-525-5p/HO-1 axis. *Commun. Biol.* **6**, 200 (2023).

38. Li, X. et al. circFNDC3B accelerates vasculature formation and metastasis in oral squamous cell carcinoma. *Cancer Res.* **83**, 1459–1475 (2023).

39. Kristensen, L. S., Jakobsen, T., Hager, H. & Kjems, J. The emerging roles of circRNAs in cancer and oncology. *Nat. Rev. Clin. Oncol.* **19**, 188–206 (2022).

40. Huang, C., Liang, D., Tatomer, D. C. & Wilusz, J. E. A length-dependent evolutionarily conserved pathway controls nuclear export of circular RNAs. *Genes Dev.* **32**, 639–644 (2018).

41. Ngo, L. H. et al. Nuclear export of circular RNA. *Nature* **627**, 212–220 (2024).

42. Li, X., Yang, L. & Chen, L. L. The biogenesis, functions, and challenges of circular RNAs. *Mol. Cell* **71**, 428–442 (2018).

43. Wang, L. et al. Circular RNA circRHOT1 promotes hepatocellular carcinoma progression by initiation of NR2F6 expression. *Mol. Cancer* **18**, 119 (2019).

44. Conn, V. M. et al. A circRNA from SEPALLATA3 regulates splicing of its cognate mRNA through R-loop formation. *Nat. Plants* **3**, 17053 (2017).

45. Liu, F. et al. Hsa_circ_0001361 promotes bladder cancer invasion and metastasis through miR-491-5p/MMP9 axis. *Oncogene* **39**, 1696–1709 (2020).

46. Garikipati, V. N. S. et al. Circular RNA CircFndc3b modulates cardiac repair after myocardial infarction via FUS/VEGF-A axis. *Nat. Commun.* **10**, 4317 (2019).

47. Roy, A. L. Pathophysiology of TFII-I: old guard wearing new hats. *Trends Mol. Med.* **23**, 501–511 (2017).

48. Linzer, N. et al. Regulation of RNA polymerase II transcription initiation and elongation by transcription factor TFII-I. *Front. Mol. Biosci.* **8**, 681550 (2021).

49. Fan, A. X. et al. Genomic and proteomic analysis of transcription factor TFII-I reveals insight into the response to cellular stress. *Nucleic Acids Res.* **42**, 7625–7641 (2014).

50. Liang, S. et al. CBX4 regulates long-form thymic stromal lymphopoietin-mediated airway inflammation through SUMOylation in house dust mite-induced asthma. *Am. J. Respir. Cell Mol. Biol.* **66**, 648–660 (2022).

51. Jansen, C. S. et al. An intra-tumoral niche maintains and differentiates stem-like CD8 T cells. *Nature* **576**, 465–470 (2019).

52. Memczak, S. et al. Circular RNAs are a large class of animal RNAs with regulatory potency. *Nature* **495**, 333–338 (2013).

53. Gao, Y., Zhang, J. & Zhao, F. Circular RNA identification based on multiple seed matching. *Brief. Bioinform.* **19**, 803–810 (2018).

54. Zhang, H. et al. CircLIFR synergizes with MSH2 to attenuate chemoresistance via MutSalpha/ATM-p73 axis in bladder cancer. *Mol. Cancer* **20**, 70 (2021).

55. Zirkel, A. & Papantonis, A. Detecting circular RNAs by RNA fluorescence in situ hybridization. *Methods Mol. Biol.* **1724**, 69–75 (2018).

Acknowledgements

Author contributions

X.W., X.X., and Z.W. designed all primers and performed all western blot assays, circFNDC3B pull-down experiments, and data analysis; S.X., W.P.,

L.Y., Y.Q., L.C., B.Y., and S.Z. performed most flow cytometry experiments, FISH assay, CCK-8 assay, transwell migration matrigel invasion assays, apoptosis assays, cell cycle assays, and animal experiments; Q.X., H.W., and J.A. analyzed and interpreted the data (e.g., statistical analysis, and bioinformatics analysis); X.W., X.X., Z.W., S.X., W.P., L.Y., K.J., and Q.Z. wrote, reviewed, and/or revised the manuscript; X.W., X.X., Z.W., K.J., and Q.Z. provided material, technical, and administrative support. All authors have read and approved the final version of the manuscript.

Competing interests
The authors declare no competing interests.

Ethics approval and consent to participate
The study was approved by the Institutional Review Board of Tongji Medical College of Huazhong University of Science and Technology on 19 July 2021, with the number 2021 IECS 0663. All animal experiments were approved by the Animal Care and Utilization Committee of Tongji Medical College, Huazhong University of Science and Technology, with the number 2021 IECS 2974. All authors consent to the publication of the manuscript.

Additional information
Supplementary information The online version contains supplementary material available at https://doi.org/10.1038/s42003-025-08108-6.

Correspondence and requests for materials should be addressed to Ke Jiang or Qiong Zhou.

Reprints and permissions information is available at http://www.nature.com/reprints

Publisher's note Springer Nature remains neutral with regard to jurisdictional claims in published maps and institutional affiliations.